

Baseline Predictions for Open and Hidden Heavy Flavor Production at RHIC II

R. Vogt

Nuclear Science Division, Lawrence Berkeley National Laboratory, Berkeley, CA 94720, USA

Physics Department, University of California, Davis, CA 95616, USA

Outline

- Open Heavy Flavor Production at RHIC
 - Theory of Heavy Flavor Production
 - Total Cross Sections and Distributions
- J/ψ and Upsilon Production at RHIC
 - Model Calculations
 - Initial and Final State Effects on J/ψ at RHIC

Charm as a Probe of Heavy Ion Collisions

Hard probe produced in the initial nucleon-nucleon collisions

Interacts strongly so its momentum can be modified by collisions during the evolution of the system leading to effects such as

- Energy loss in dense matter (Djordjevic et al, Lin et al, Kharzeev and Dokshitzer)
- Transverse momentum broadening due to hadronization from quark-gluon plasma (Svetitsky) or cold nuclear matter
- Collective flow of charm quarks (Lin and Molnar, Rapp et al)

In addition, if multiple $c\bar{c}$ pairs are produced in a given event, can enhance J/ψ (hidden charm) production (Thews et al)

pp and d+Au collisions serve as an important baseline for understanding medium effects on charm production, need good theoretical background and up-to-date open charm data

Charm Hadrons

Open charm hadron production and decay can be detected both through lepton channels (semi-leptonic decays) and through pure hadronic channels (reconstruction of the D mass, momentum)

Table shows that measuring D mesons alone is not enough to get total $c\bar{c}$ cross section

C	Mass (GeV)	$c\tau$ (μm)	$B(C \rightarrow lX)$ (%)	$B(C \rightarrow \text{Hadrons})$ (%)
$D^+(c\bar{d})$	1.869	315	17.2	$K^-\pi^+\pi^+$ (9.1)
$D^-(\bar{c}d)$	1.869	315	17.2	$K^+\pi^-\pi^-$ (9.1)
$D^0(c\bar{u})$	1.864	123.4	6.87	$K^-\pi^+$ (3.8)
$\overline{D^0}(\bar{c}u)$	1.864	123.4	6.87	$K^+\pi^-$ (3.8)
$D^{*\pm}$	2.010			$D^0\pi^\pm$ (67.7), $D^\pm\pi^0$ (30.7)
D^{*0}	2.007			$D^0\pi^0$ (61.9)
$D_s^+(c\bar{s})$	1.969	147	8	$K^+K^-\pi^+$ (4.4), $\pi^+\pi^+\pi^-$ (1.01)
$D_s^-(\bar{c}s)$	1.969	147	8	$K^+K^-\pi^-$ (4.4), $\pi^+\pi^-\pi^-$ (1.01)
$\Lambda_c^+(udc)$	2.285	59.9	4.5	ΛX (35), $pK^-\pi^+$ (2.8)
$\Sigma_c^{++}(uuc)$	2.452			$\Lambda_c^+\pi^+$ (100)
$\Sigma_c^+(udc)$	2.451			$\Lambda_c^+\pi^0$ (100)
$\Sigma_c^0(ddc)$	2.452			$\Lambda_c^+\pi^-$ (100)
$\Xi_c^+(usc)$	2.466	132		$\Sigma^+K^-\pi^+$ (1.18)
$\Xi_c^0(dsc)$	2.472	29		$\Xi^-\pi^+$ (seen)

Table 1: Ground state charm hadrons with their mass, decay length (when given) and branching ratios to leptons (when applicable) and some prominent decays to hadrons, preferably to only charged hadrons although such decays are not always available.

Bottom Hadrons

Open bottom production and decay can also be detected both through lepton channels (semi-leptonic decays) and through pure hadronic channels (reconstruction of the B mass, momentum)

J/ψ decay channel is often used to obtain B cross section since J/ψ is “easy” to detect

Hadronic branching ratios small, two body decays to charged hadrons rare

B decays contribute to lepton spectra in two ways: direct $B \rightarrow lX$ and the indirect chain decay $B \rightarrow DX \rightarrow lX'$

Not much information available on bottom baryons

C	Mass (GeV)	$c\tau$ (μm)	$B(C \rightarrow lX)$ (%)	$B(C \rightarrow \text{Hadrons})$ (%)
$B^+(u\bar{b})$	5.2790	501	10.2	$\bar{D}^0 \pi^- \pi^+ \pi^+$ (1.1), $J/\psi K^+$ (0.1)
$B^-(\bar{u}b)$	5.2790	501	10.2	$D^0 \pi^+ \pi^- \pi^-$ (1.1), $J/\psi K^-$ (0.1)
$B^0(d\bar{b})$	5.2794	460	10.5	$D^- \pi^+$ (0.276), $J/\psi K^+ \pi^-$ (0.0325)
$\bar{B}^0(\bar{d}b)$	5.2794	460	10.5	$D^+ \pi^-$ (0.276), $J/\psi K^- \pi^+$ (0.0325)
B_s^0	5.3696	438		$D_s^- \pi^+$ (< 13)
$B_c^+(c\bar{b})$	6.4			$J/\psi \pi^+$ (0.0082)
$B_c^-(\bar{c}b)$	6.4			$J/\psi \pi^-$ (0.0082)
$\Lambda_b^0(udb)$	5.624	368		$J/\psi \Lambda$ (0.047), $\Lambda_c^+ \pi^-$ (seen)

Table 2: Known ground state bottom hadrons with their mass, decay length (when given), branching ratios to leptons (when applicable) and some selected decays to hadrons.

Calculating Heavy Flavors in Perturbative QCD

‘Hard’ processes have a large scale in the calculation that makes perturbative QCD applicable: high momentum transfer, μ^2 , high mass, m , high transverse momentum, p_T , since $m \neq 0$, heavy quark production is a ‘hard’ process

Asymptotic freedom assumed to calculate the interactions between two hadrons on the quark/gluon level but the confinement scale determines the probability of finding the interacting parton in the initial hadron

Factorization assumed between the perturbative hard part and the universal, nonperturbative parton distribution functions

The hadronic cross section in an AB collision where $AB = pp, pA$ or nucleus-nucleus is

$$\begin{aligned} \sigma_{AB}(S, m^2) = & \sum_{i,j=q,\bar{q},g} \int_{4m_Q^2/s}^1 \frac{d\tau}{\tau} \int dx_1 dx_2 \delta(x_1 x_2 - \tau) \\ & \times f_i^A(x_1, \mu_F^2) f_j^B(x_2, \mu_F^2) \hat{\sigma}_{ij}(s, m^2, \mu_F^2, \mu_R^2) \end{aligned}$$

f_i^A are the nonperturbative parton distributions, determined from fits to data, x_1 and x_2 are the fractional momentum of hadrons A and B carried by partons i and j , $\tau = s/S$

$\hat{\sigma}_{ij}(s, m^2, \mu_F^2, \mu_R^2)$ is hard partonic cross section calculable in QCD in powers of α_s^{2+n} : leading order (LO), $n = 0$; next-to-leading order (NLO), $n = 1 \dots$

Results depend strongly on quark mass, m , factorization scale, μ_F , in the parton densities and renormalization scale, μ_R , in α_s

Calculating the Total Cross Sections

Partonic total cross section only depends on quark mass m , not kinematic quantities
To NLO

$$\begin{aligned}\hat{\sigma}_{ij}(s, m, \mu_F^2, \mu_R^2) &= \frac{\alpha_s^2(\mu_R^2)}{m^2} \left\{ f_{ij}^{(0,0)}(\rho) \right. \\ &\quad \left. + 4\pi\alpha_s(\mu_R^2) \left[f_{ij}^{(1,0)}(\rho) + f_{ij}^{(1,1)}(\rho) \ln(\mu_F^2/m^2) \right] + \mathcal{O}(\alpha_s^2) \right\}\end{aligned}$$

$\rho = 4m^2/s$, s is partonic center of mass energy squared

μ_F is factorization scale, separates hard part from nonperturbative part

μ_R is renormalization scale, scale at which strong coupling constant α_s is evaluated

$\mu_F = \mu_R$ in evaluations of parton densities

$f_{ij}^{(a,b)}$ are dimensionless, μ -independent scaling functions, $a = 0, b = 0$ and $ij = q\bar{q}, gg$ for LO, $a = 1, b = 0, 1$ and $ij = q\bar{q}, gg$ and $qg, \bar{q}g$ for NLO

$f_{ij}^{(0,0)}$ are always positive, $f_{ij}^{(1,b)}$ can be negative also

Note that if $\mu_F^2 = m^2$, $f_{ij}^{(1,1)}$ does not contribute

Scaling Functions to NLO

Near threshold, $\sqrt{s}/2m \rightarrow 1$, Born contribution is large but dies away for $\sqrt{s}/2m \rightarrow \infty$

At large $\sqrt{s}/2m$, gg channel is dominant, then qg

High energy behavior of the cross sections due to phase space and low x behavior of parton densities

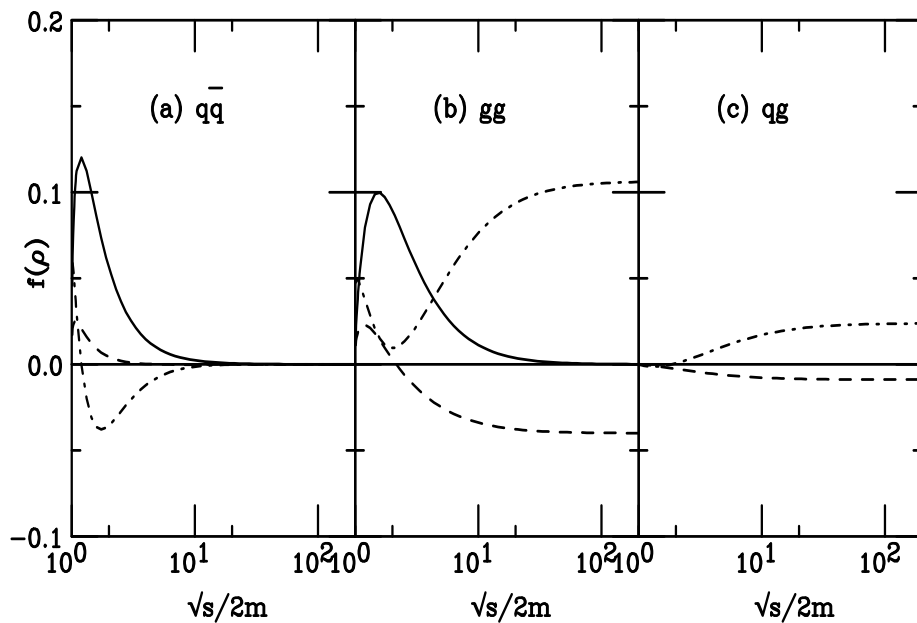


Figure 1: Scaling functions needed to calculate the total partonic $Q\bar{Q}$ cross section. The solid curves are the Born results, $f_{ij}^{(0,0)}$, the dashed and dot-dashed curves are NLO contributions, $f_{ij}^{(1,1)}$ and $f_{ij}^{(1,0)}$ respectively.

Comparison of $c\bar{c}$ Calculations to Data

Two ways to evaluate total cross sections and make predictions for higher energies

There are only 2 important parameters at fixed target energies: the quark mass m and the scale μ – at higher energies, the low x , low μ behavior of the parton densities plays an important role in the asymptotic result

The scale is usually chosen so that $\mu_F = \mu_R$, as in parton density fits although there is no strict reason for doing so for heavy flavors

First way (RV, Hard Probes Collaboration): fix m and $\mu \equiv \mu_F = \mu_R \geq m$ to data at lower energies and extrapolate to unknown regions – tends to favor lower masses

Second way (Cacciari, Nason and RV): determine an uncertainty band within $1.3 < m < 1.7$ GeV for charm and $4.5 < m < 5$ GeV for bottom with $(\mu_F/m, \mu_R/m) = (1, 1), (2, 2), (0.5, 0.5), (0.5, 1), (1, 0.5), (1, 2), (2, 1)$

We have to be careful with the resulting total charm cross sections for $\mu_F \leq m$ with the CTEQ6M parton densities since the minimum μ is 1.3 GeV, giving us big K factors for the lower scales and making the use of $\mu_F \leq m$ problematic, to say the least!

Densities like GRV98 have a lower starting scale, making their behavior for low x , low μ charm production less problematic

Note also that even the two-loop evaluation of α_s is big for low scales, for $m = 1.5$ GeV:

$$\alpha_s(m/2 = 0.75) = 0.648, \alpha_s(m = 1.5) = 0.348 \text{ and } \alpha_s(2m = 3) = 0.246$$

CTEQ6M Densities at $\mu = m/2, m$ and $2m$

CTEQ6M densities extrapolate to $\mu < \mu_{\min} = 1.3$ GeV

When backwards extrapolation leads to $xg(x, \mu) < 0$, then $xg(x, \mu) \equiv 0$

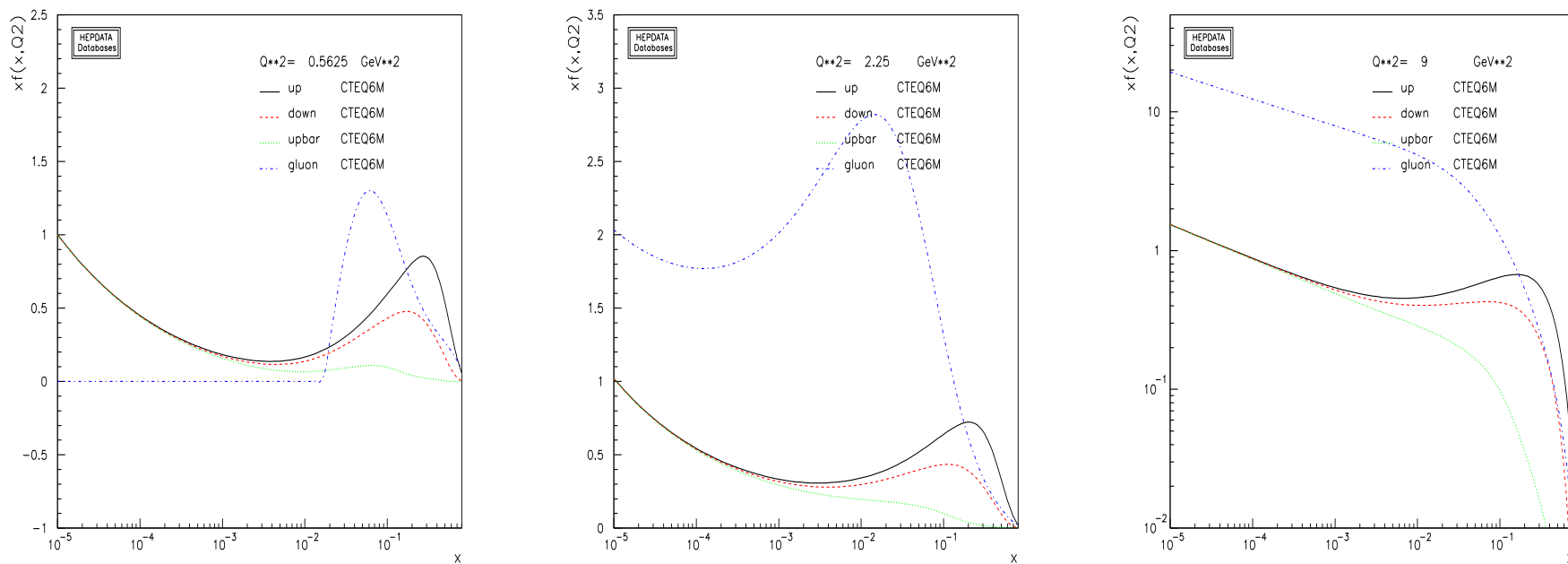


Figure 2: The CTEQ6M parton densities as a function of x for $\mu = m/2$ (left), $\mu = m$ (middle) and $\mu = 2m$ (right) for $m = 1.5$ GeV.

Fixing m and μ^2 to All Data: Method 1

Difficult to obtain a large calculated $c\bar{c}$ cross section with $\mu_F^2 = \mu_R^2$, as in parton density fits

Data favors lower masses – lowest mass used here is 1.2 GeV but much lower masses than allowed in pQCD needed to agree with largest cross sections

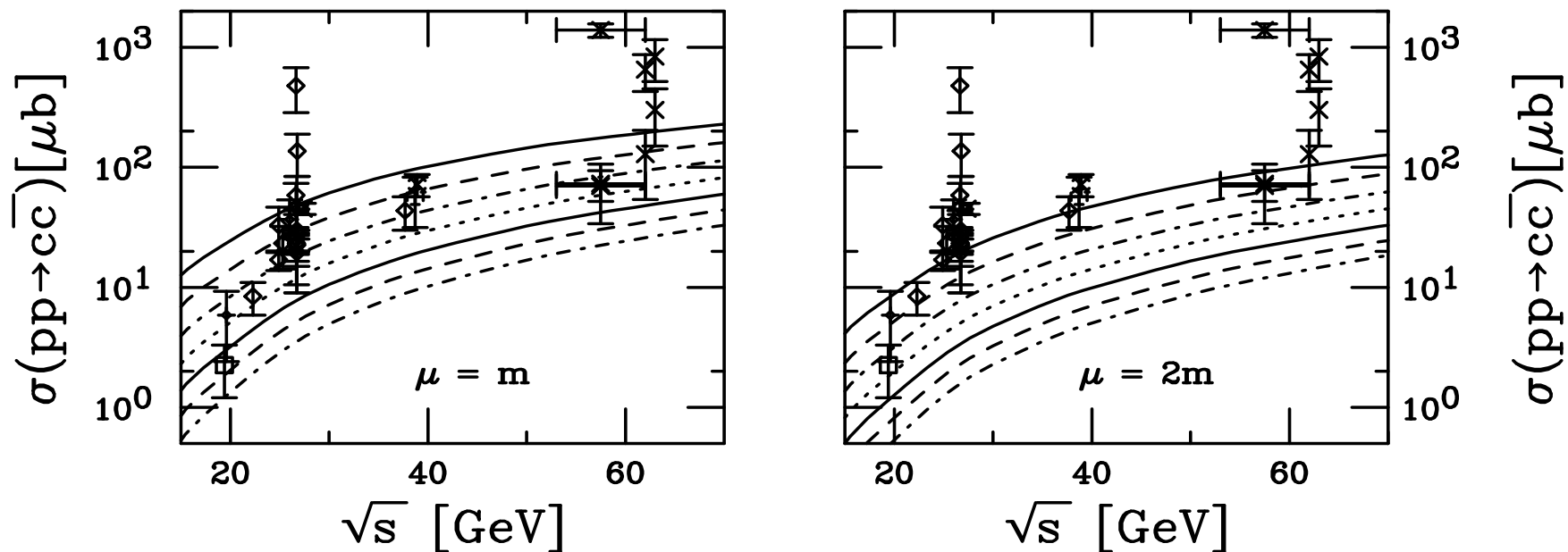


Figure 3: Total $c\bar{c}$ cross sections in pp and pA interactions up to ISR energies as a function of the charm quark mass using the CTEQ6M parton densities. The left-hand plot shows the results with $\mu_F = \mu_R = m$ while in the right-hand plot $\mu_F = \mu_R = 2m$. From top to bottom the curves are $m = 1.2, 1.3, 1.4, 1.5, 1.6, 1.7, 1.8$ GeV.

Extrapolation to Higher Energies

We have kept only the most recent measurements, including the PHENIX $\sqrt{S} = 130$ GeV result from Au+Au, lowest $\sqrt{S} = 200$ GeV point is from PHENIX pp

Note the $\mu = m$ behavior at high energy: the cross section grows slower with \sqrt{s} due to the small x behavior of $xg(x, \mu)$ for μ close to μ_{\min}

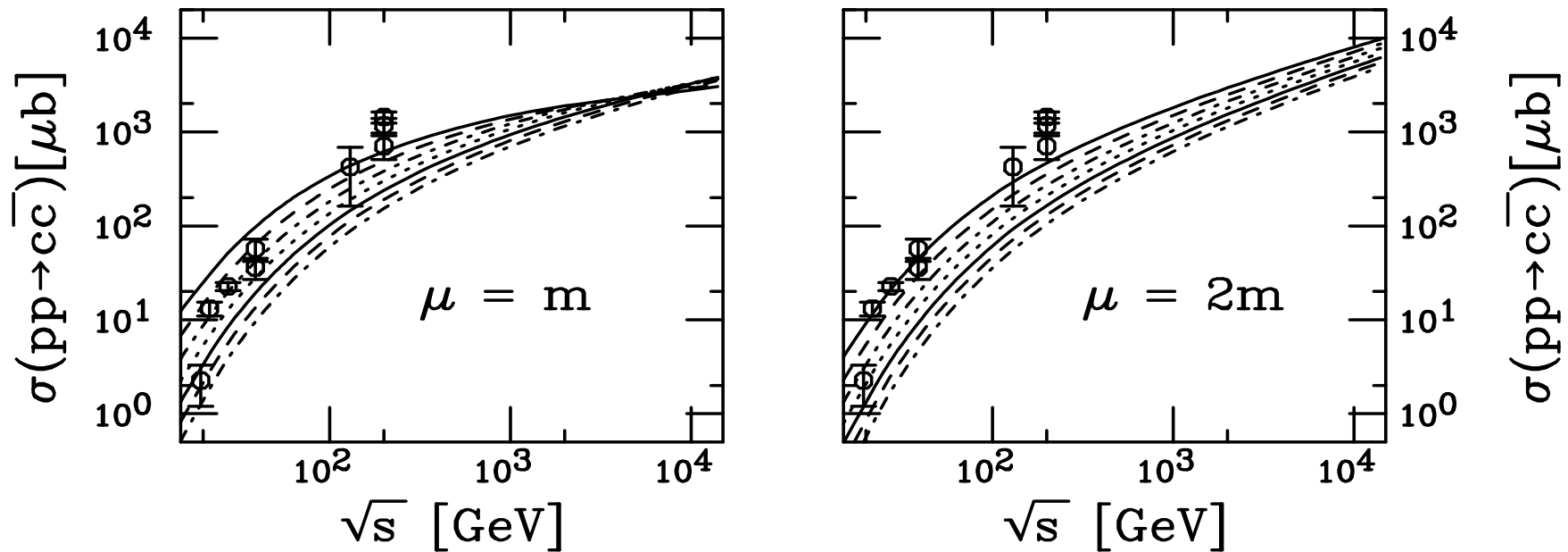


Figure 4: Same as previous but the energy range extended to LHC energies.

K Factors Using Method 1

K factors defined here as the ratio of the NLO to LO cross sections, both calculated with NLO parton densities and two loop evaluation of α_s

Note the $\mu = m$ behavior at high energy – K factors grow at low mass and then turn over due to both the low x parton densities and the fact that the LO cross section gets small far from threshold

The larger the value of μ , the better behaved the K factors

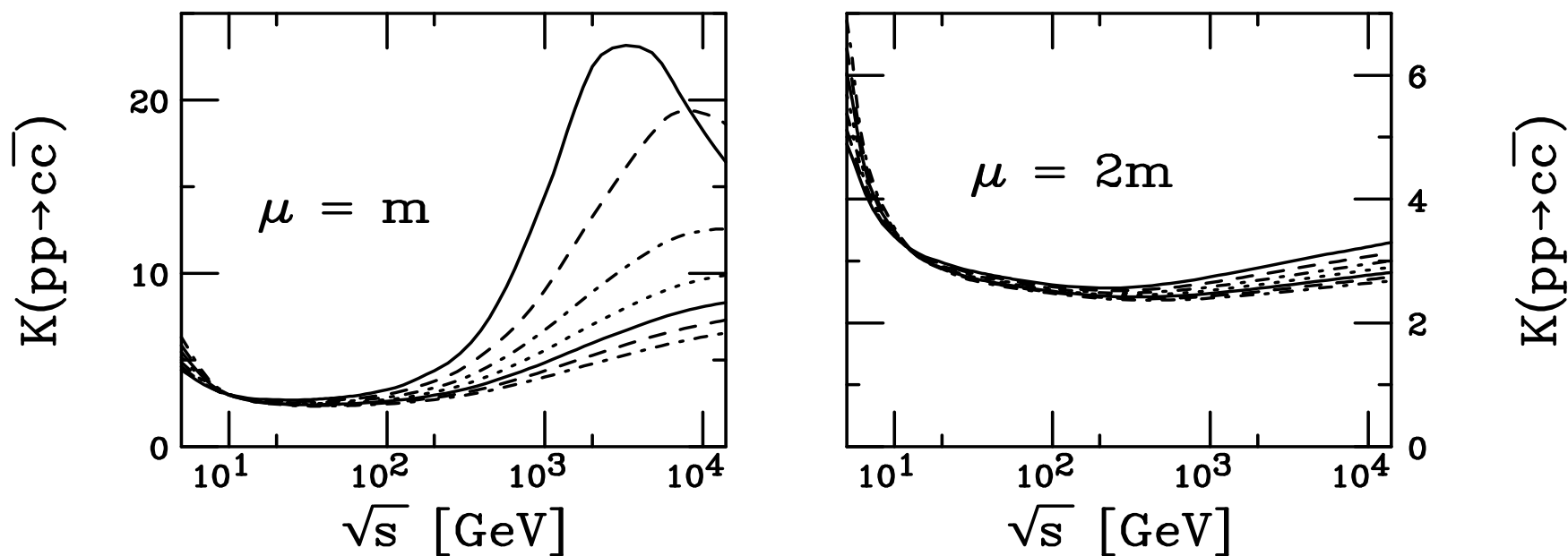


Figure 5: The K factors over the full \sqrt{s} range.

Theoretical Uncertainty Band: Method 2

Curves with $(\mu_F/m, \mu_R/m) = (1, 0.5)$ and $(0.5, 0.5)$ have large total cross sections since $\alpha_s(m/2) = 0.648$, really too high to get a convergent result

Curves with $\mu_F \leq m$ turn over for $\sqrt{s} > 100$ GeV due to low x , low μ behavior of parton densities

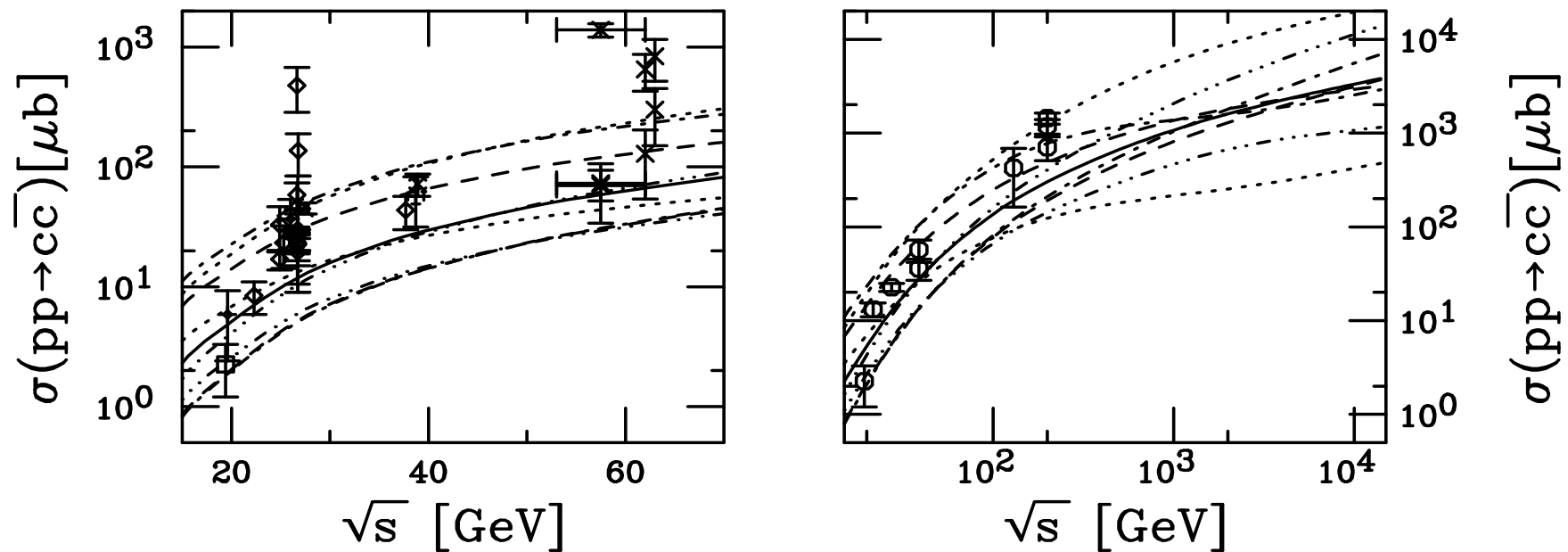


Figure 6: Total $c\bar{c}$ cross sections calculated using CTEQ6M. The solid curve is the central value $(\mu_F/m, \mu_R/m) = (1, 1)$ with $m = 1.5$ GeV. The upper and lower dashed curves are $m = 1.3$ and 1.7 GeV with $(1, 1)$ respectively. The upper and lower dot-dashed curves correspond to $(0.5, 0.5)$ and $(2, 2)$ while the upper and lower dotted curves are with $(1, 0.5)$ and $(0.5, 1)$ with $m = 1.5$ GeV.

Theoretical Uncertainty Band: K Factors

Results with $(\mu_F/m, \mu_R/m) = (1, 0.5)$ and $(0.5, 0.5)$ have largest K factors

Results with $(1, 1)$, $(2, 2)$, $(2, 1)$ and $(1, 2)$ with $m = 1.5$ GeV and $(1, 1)$ with $m = 1.7$ GeV give $K < 10$ at highest energies

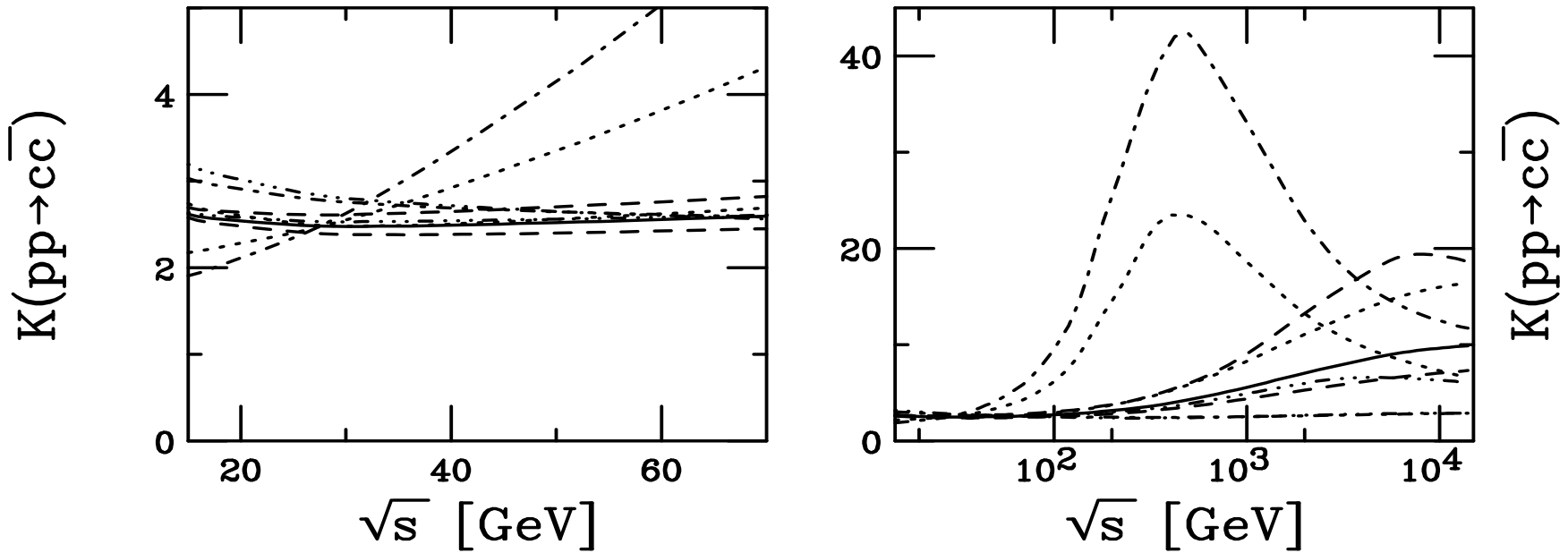


Figure 7: The $c\bar{c}$ K factors calculated using CTEQ6M. The solid curve is the central value $(\mu_F/m, \mu_R/m) = (1, 1)$ with $m = 1.5$ GeV. The upper and lower dashed curves are $m = 1.3$ and 1.7 GeV with $(1, 1)$ respectively. The upper and lower dot-dashed curves correspond to $(0.5, 0.5)$ and $(2, 2)$ while the upper and lower dotted curves are with $(1, 0.5)$ and $(0.5, 1)$ with $m = 1.5$ GeV.

Comparison of Bottom Calculations to Data

Fewer data on bottom production in pp collisions, especially on total cross section

Bottom production is less problematic because, even for $\mu = m/2$, we are well above μ_{\min} of parton densities, extrapolation to higher energies should also be better

Fixing m and μ^2 to All Data: Method 1

Latest HERA-B point not shown, lies below previous point

In this approach, $m = 5$ GeV, $\mu = m/2$; $m = 4.75$ GeV, $\mu = m$; and $m = 4.5$ GeV, $\mu = 2m$ are all close to center of data

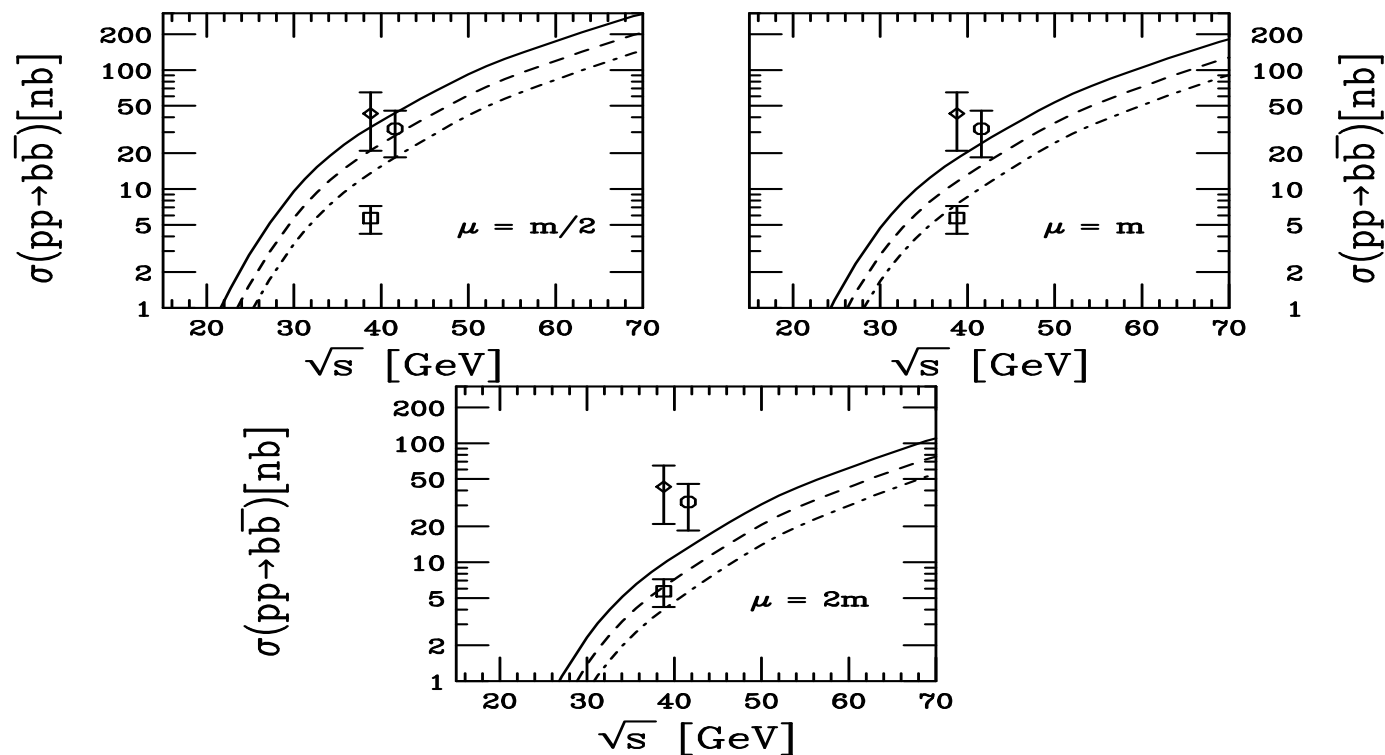


Figure 8: Total $b\bar{b}$ cross sections in pp and pA interactions as a function of the bottom quark mass using the CTEQ6M parton densities. Clockwise from upper left, the plots give results for $\mu = m/2$, $\mu = m$ and $\mu = 2m$. The mass values are 4.5 GeV (solid), 4.75 GeV (dashed) and 5 GeV (dot-dashed).

Extrapolation to Higher Energies

Asymptotic behavior very similar for bottom, no surprises

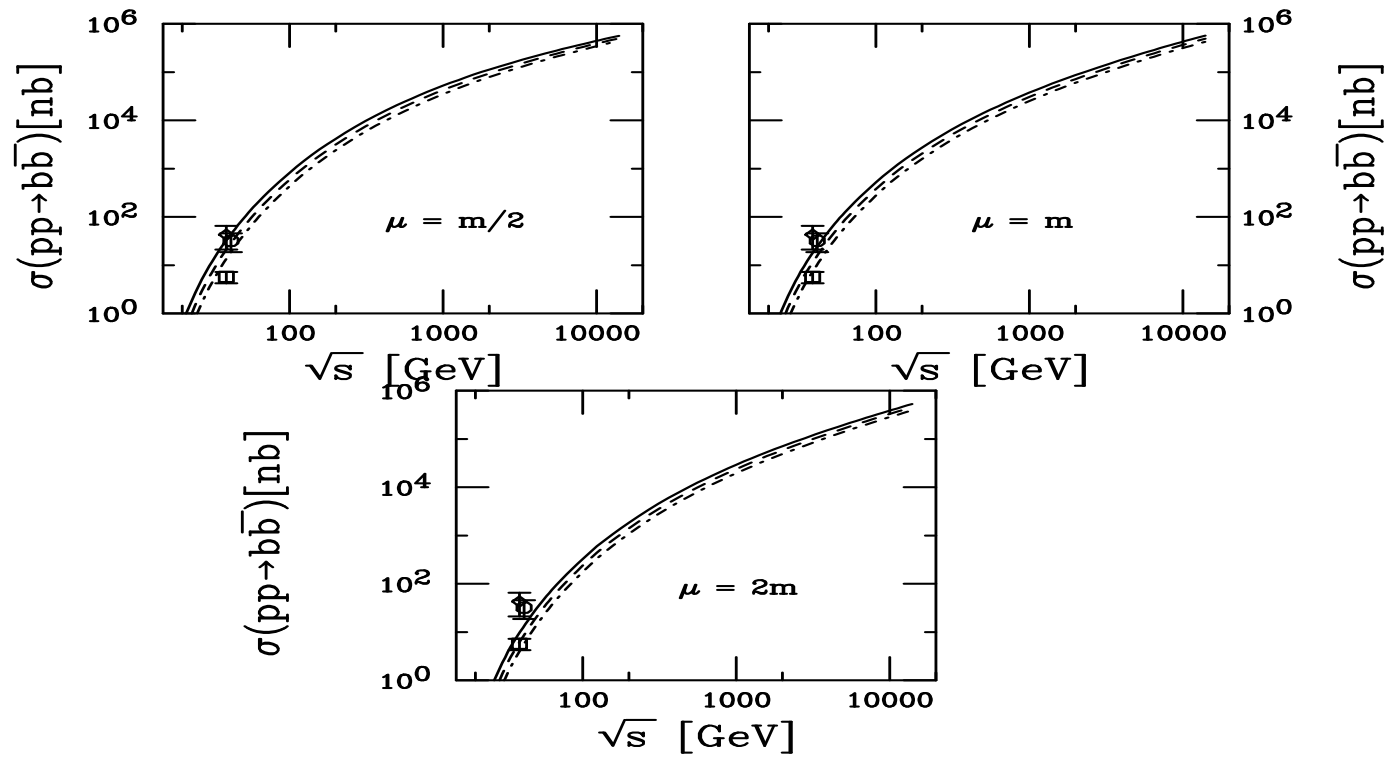


Figure 9: Same as previous but the energy range extended to LHC energies.

K Factors Using Method 1

K factors better behaved for bottom production, x and μ not so small as for charm, consequently α_s is smaller also

K factors much smaller at higher energy than charm, strong growth only seen for $\mu = m/2$, smallest K factors for $\mu = 2m$, also the case with charm

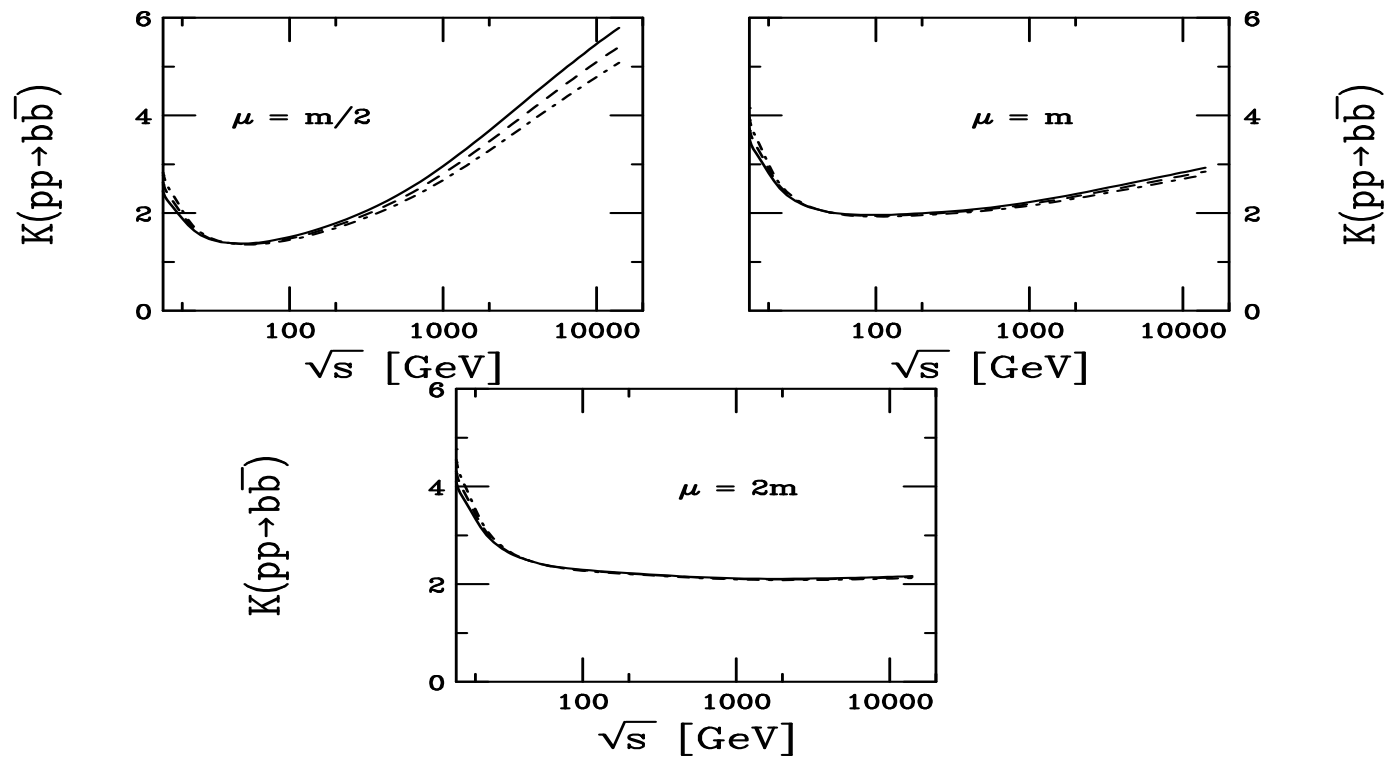


Figure 10: The K factors over the full \sqrt{s} range.

Theoretical Uncertainty Band: Method 2

More sensible to talk about uncertainty band for bottom than for charm

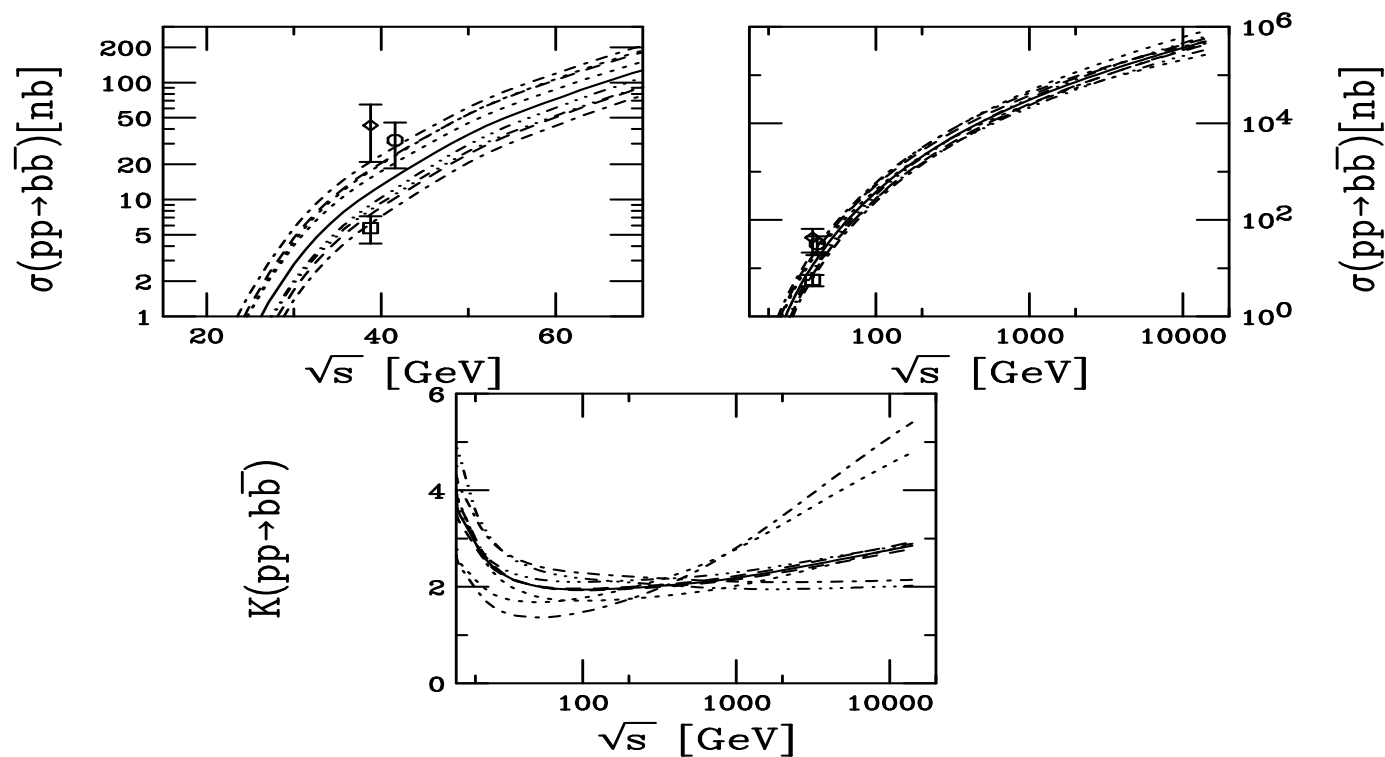


Figure 11: Total $b\bar{b}$ cross sections calculated using CTEQ6M. The solid curve is the central value $(\mu_F/m, \mu_R/m) = (1, 1)$ with $m = 4.75$ GeV. The upper and lower dashed curves are $m = 4.5$ and 5 GeV with $(1, 1)$ respectively. The upper and lower dot-dashed curves correspond to $(0.5, 0.5)$ and $(2, 2)$ while the upper and lower dotted curves are with $(1, 0.5)$ and $(0.5, 1)$ with $m = 4.75$ GeV. (The upper dotted curve is similar to the upper dashed curve at low energies.)

From Total Cross Sections to Distributions

Distributions as a function of kinematic variables can provide more information than the total cross section

In total cross section, the quark mass is the only relevant scale

When considering kinematic observables like x_F or p_T , the momentum scale is also relevant so that, instead of $\mu^2 \propto m^2$, one usually uses $\mu^2 \propto m_T^2$ – this difference makes the p_T -integrated total cross section decrease a bit relative to that calculated using the dimensionless scaling functions

Fragmentation also important when discussing observables

Fragmentation universal, like parton densities, so the parameterizations of e^+e^- data should work in hadroproduction – new determinations of the charm to D fragmentation in Mellin space result in a softer, more accurate spectra than the old Peterson function

NLO Bare Quark p_T Distributions

Differences largest at low p_T , determines total cross section

Distributions become similar at high p_T

Average p_T increases with m and decreases with μ

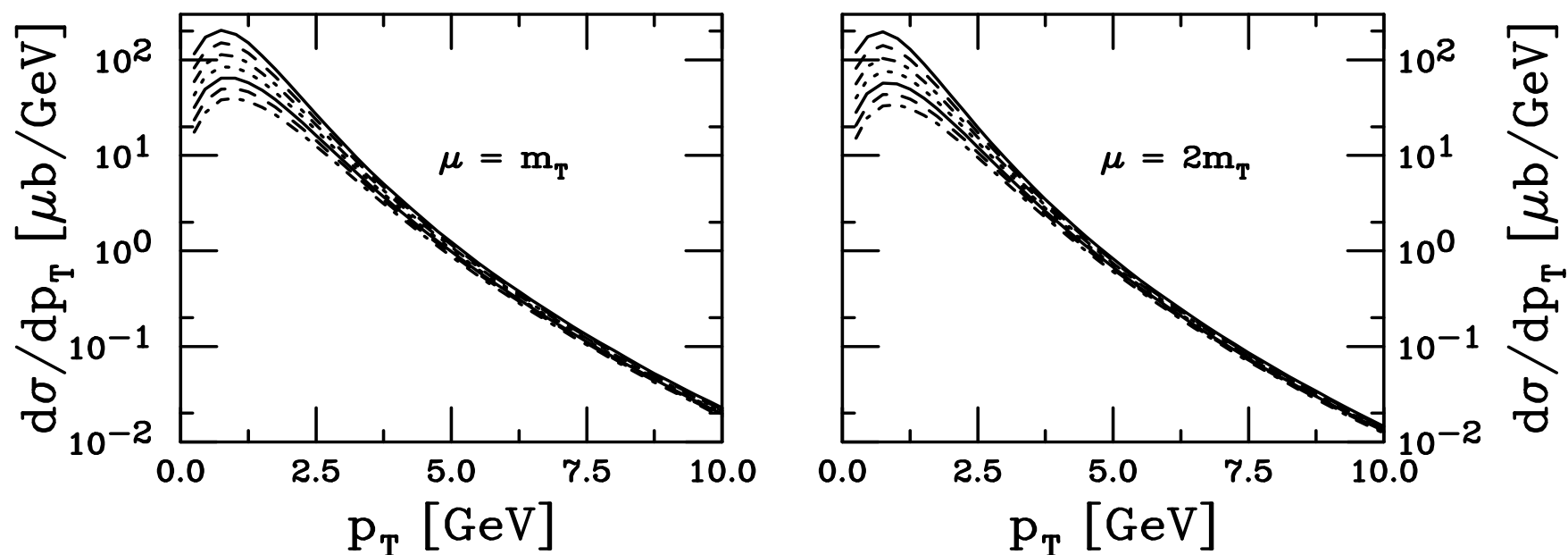


Figure 12: The NLO charm quark p_T distributions in pp interactions at $\sqrt{S} = 200$ GeV as a function of the charm quark mass calculated with the GRV98 HO parton densities, integrated over all rapidity. The left-hand plot shows the results with the renormalization and factorization scales equal to m_T while in the right-hand plot the scale is set to $2m_T$. From top to bottom the curves are $m = 1.2, 1.3, 1.4, 1.5, 1.6, 1.7,$ and 1.8 GeV.

FONLL Calculation of p_T Dependence (Cacciari and Nason)

Designed to cure large logs of p_T/m for $p_T \gg m$ in fixed order calculation (FO) where mass is no longer only relevant scale

Includes resummed terms (RS) of order $\alpha_s^2(\alpha_s \log(p_T/m))^k$ (leading log – LL) and $\alpha_s^3(\alpha_s \log(p_T/m))^k$ (NLL) while subtracting off fixed order terms retaining only the logarithmic mass dependence (the “massless” limit of fixed order (FOM0)), both calculated in the same renormalization scheme

There needs to be a scheme change in the FO calculation since it treats the heavy flavor as heavy while the RS approach includes the heavy flavor as an active light degree of freedom

Schematically then:

$$\text{FONLL} = \text{FO} + (\text{RS} - \text{FOM0})G(m, p_T)$$

The function $G(m, p_T)$ is arbitrary but must approach unity as $m/p_T \rightarrow 0$ up to terms suppressed by powers of m/p_T

Total cross section similar to but slightly higher than NLO

One drawback: problems with matching arise at larger rapidity, therefore we don't calculate results for $|y| > 2$

Comparison of FONLL and NLO p_T Distributions

FONLL result for bare charm is slightly higher over most of the p_T range – fixed order result gets higher at large p_T due to large $\log(p_T/m)$ terms

New fragmentation functions (dashed curve) for D^0 harder than Peterson function (dot-dot-dot-dashed curve)

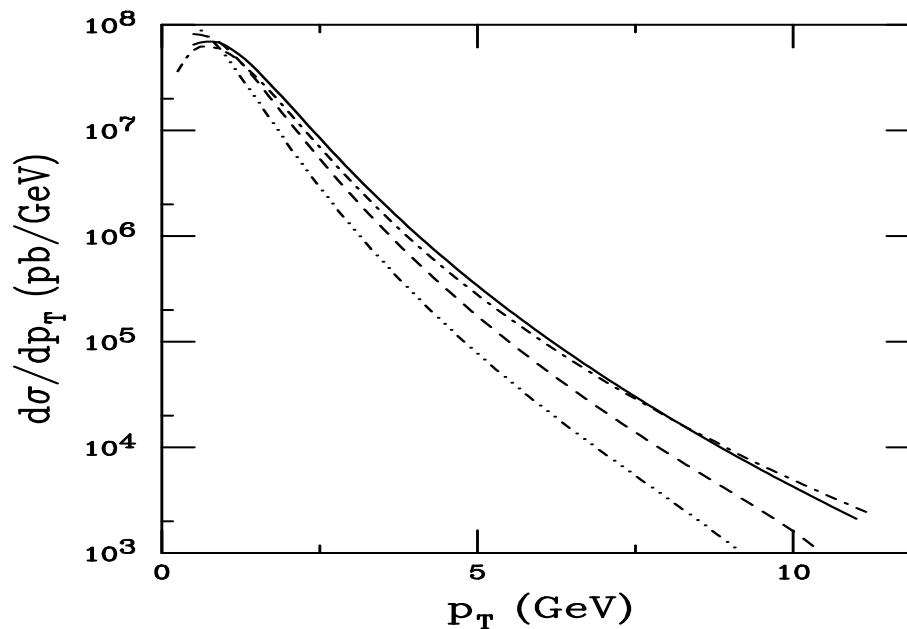


Figure 13: The p_T distributions calculated using FONLL are compared to NLO. The dot-dashed curve is the NLO charm quark p_T distribution. The solid, dashed and dot-dot-dot-dashed curves are FONLL results for the charm quark and D^0 meson with the updated fragmentation function and the Peterson function, respectively. All the calculations are done with the CTEQ6M parton densities, $m = 1.2$ GeV and $\mu = m_T$ in the region $|y| \leq 0.75$.

Uncertainty Bands for p_T Distributions

As we saw for the total cross sections, depending on μ_R , μ_F and m , the maximum and minimum values of the calculated total cross section may come from different curves

Same is true for p_T distributions: upper and lower curves in the band do not represent a single set of μ_R , μ_F and m values but are the upper and lower limits of mass and scale uncertainties added in quadrature:

$$\begin{aligned}(d\sigma/dp_T)_{\max} &= (d\sigma/dp_T)_{\text{central}} + \sqrt{((d\sigma/dp_T)_{\mu,\max} - (d\sigma/dp_T)_{\text{central}})^2 + ((d\sigma/dp_T)_{m,\max} - (d\sigma/dp_T)_{\text{central}})^2} \\(d\sigma/dp_T)_{\min} &= (d\sigma/dp_T)_{\text{central}} - \sqrt{((d\sigma/dp_T)_{\mu,\min} - (d\sigma/dp_T)_{\text{central}})^2 + ((d\sigma/dp_T)_{m,\min} - (d\sigma/dp_T)_{\text{central}})^2}\end{aligned}$$

The central value is $m = 1.5$ GeV, $\mu_F = \mu_R = m_T$

We follow the same procedure for both the NLO and FONLL calculations and compare them in the central ($|y| \leq 0.75$) and forward ($1.2 < y < 2.2 - 1.2 < y < 2$ for FONLL) regions

Previous results with $m = 1.2$ GeV, $\mu_F = \mu_R = 2m_T$ fall within the uncertainty band

We give results for bare heavy flavors and heavy flavor mesons in pp collisions at $\sqrt{s} = 200$ and 500 GeV

Note that, due to the scale change from m to m_T in the p_T distributions leads to much lower integrated total cross sections for $(\mu_F/m_T, \mu_R/m_T) = (1, 0.5)$ and $(0.5, 0.5)$ since $\alpha_s(m_T)$ decreases with p_T

Components of Uncertainty Band at NLO

Curves with $(\mu_F/m_T, \mu_R/m_T) = (1, 0.5)$ and $(0.5, 0.5)$ make up the upper scale uncertainty while those with $(0.5, 1)$ and $(2, 2)$ make up the lower

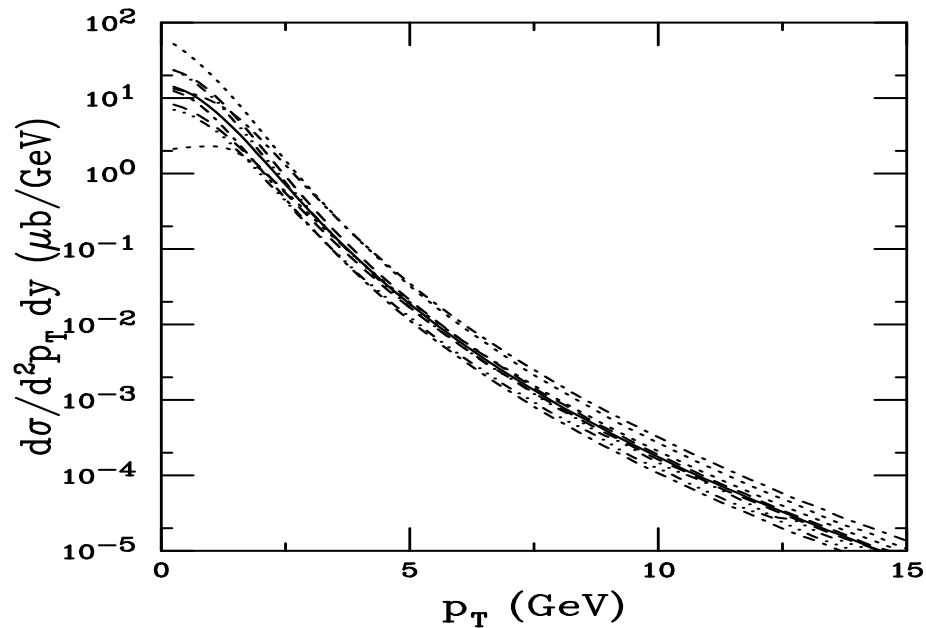


Figure 14: The charm quark p_T distributions calculated using CTEQ6M. The solid curve is the central value $(\mu_F/m_T, \mu_R/m_T) = (1, 1)$ with $m = 1.5$ GeV. The upper and lower dashed curves are $m = 1.3$ and 1.7 GeV with $(1, 1)$ respectively. The upper and lower dot-dashed curves correspond to $(0.5, 0.5)$ and $(2, 2)$ while the upper and lower dotted curves are with $(1, 0.5)$ and $(0.5, 1)$ and the upper and lower dot-dot-dot-dashed curves are with $(2, 1)$ and $(1, 2)$ with $m = 1.5$ GeV.

Uncertainty Bands for c and D at 200 GeV

NLO and FONLL bands almost indistinguishable from each other, slight difference in normalization between the two at forward rapidities due to limitations on FONLL at large rapidity

D meson band uses primary D distributions, not distinguishing charged from neutral D mesons, not possible to separate c and D bands for $p_T < 10$ GeV

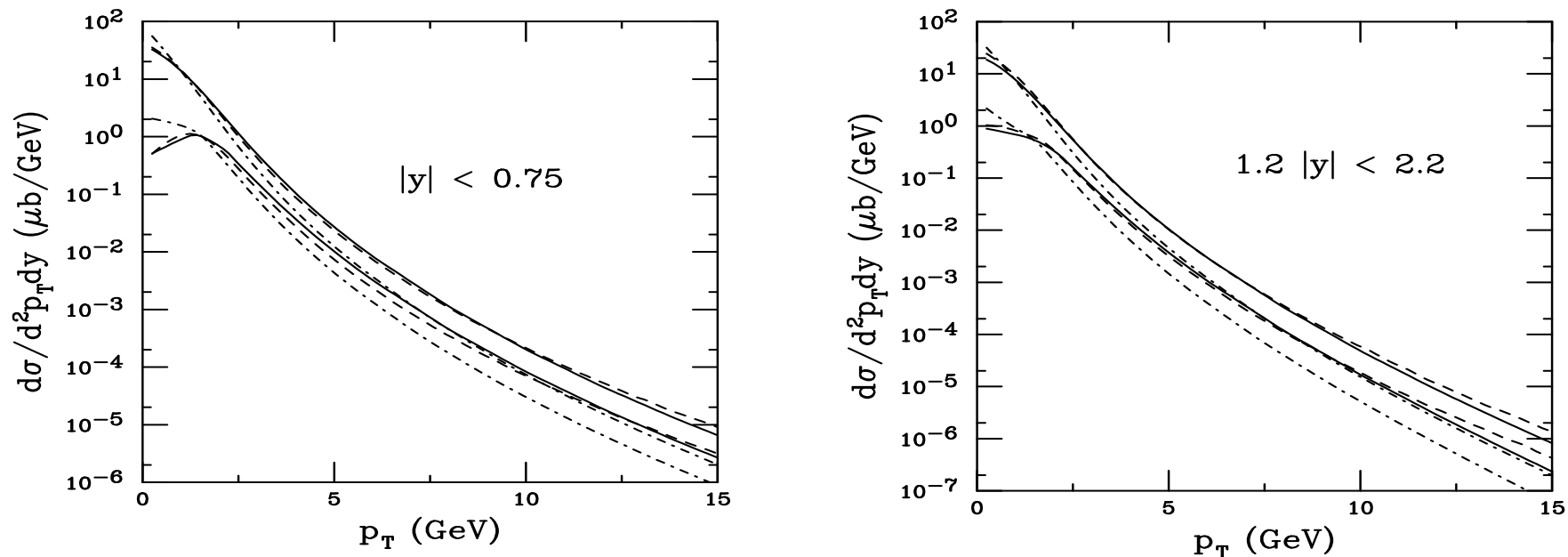


Figure 15: The charm quark theoretical band as a function of p_T for FONLL (solid curves) and NLO (dashed curves) in $\sqrt{s} = 200$ GeV pp collisions. Also shown is the D meson uncertainty band, all using the CTEQ6M parton densities. The left-hand plot gives the result for $|y| \leq 0.75$ while the right-hand plot shows the result for $1.2 \leq |y| \leq 2.2$.

Uncertainty Bands for c and D at 500 GeV

c and D distributions are harder at 500 GeV

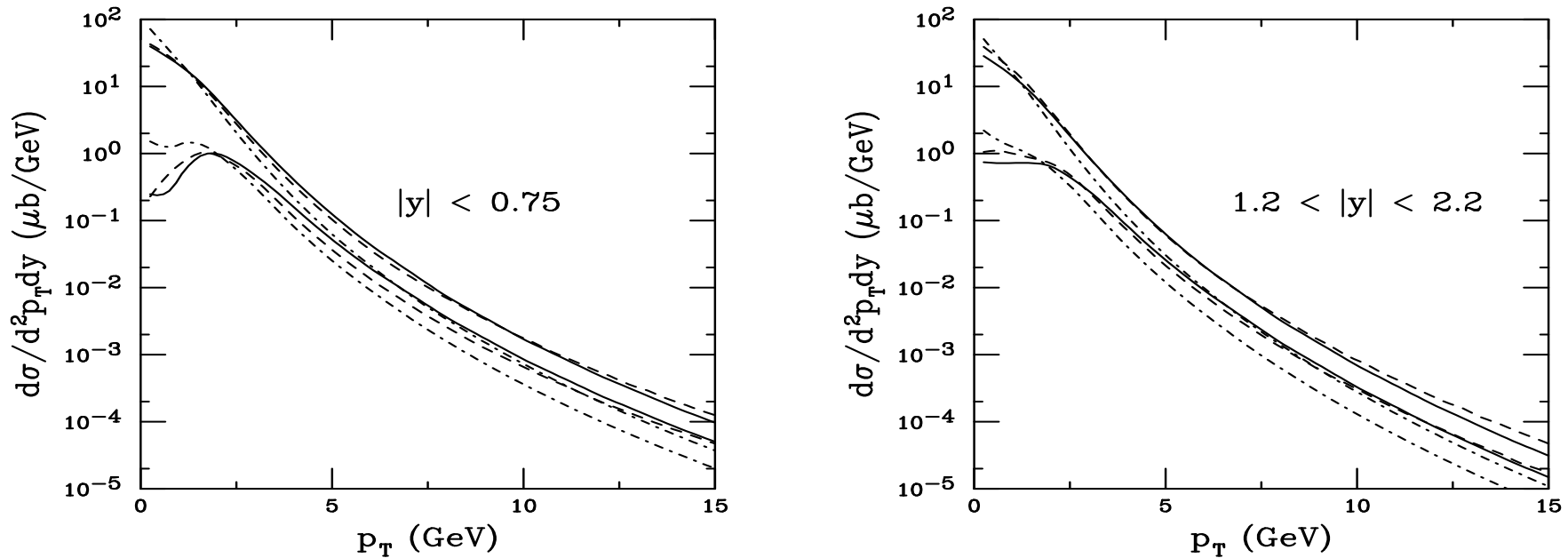


Figure 16: The charm quark theoretical band as a function of p_T for FONLL (solid curves) and NLO (dashed curves) in $\sqrt{s} = 500$ GeV pp collisions. Also shown is the D meson uncertainty band, all using the CTEQ6M parton densities. The left-hand plot gives the result for $|y| \leq 0.75$ while the right-hand plot shows the result for $1.2 \leq |y| \leq 2.2$.

Uncertainty Bands for b and B at 200 GeV

Bands narrower for bottom than for charm and impossible to separate b from B over the p_T range shown (B is a generic B meson)

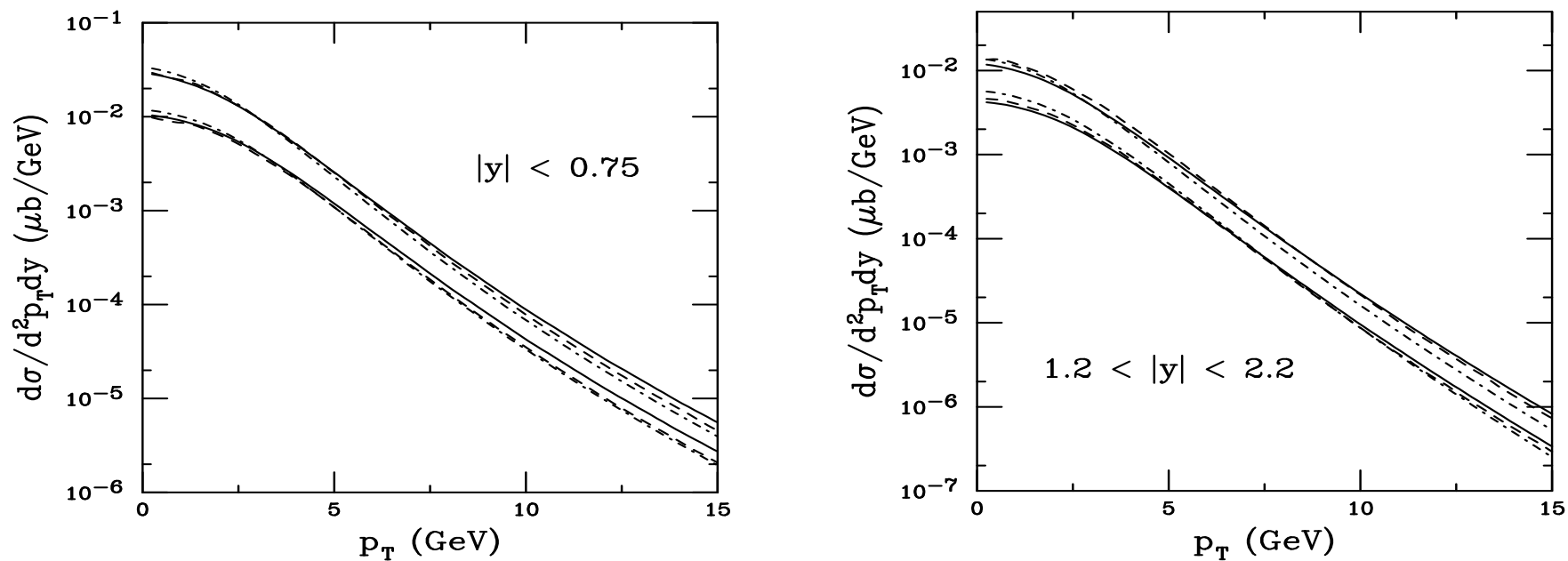


Figure 17: The bottom quark theoretical band as a function of p_T for FONLL (solid curves) and NLO (dashed curves) in $\sqrt{s} = 200$ GeV pp collisions. Also shown is the B meson uncertainty band, all using the CTEQ6M parton densities. The left-hand plot gives the result for $|y| \leq 0.75$ while the right-hand plot shows the result for $1.2 \leq |y| \leq 2.2$.

Uncertainty Bands for b and B at 500 GeV

Much stronger energy dependence and more hardening for bottom than for charm with increasing energy

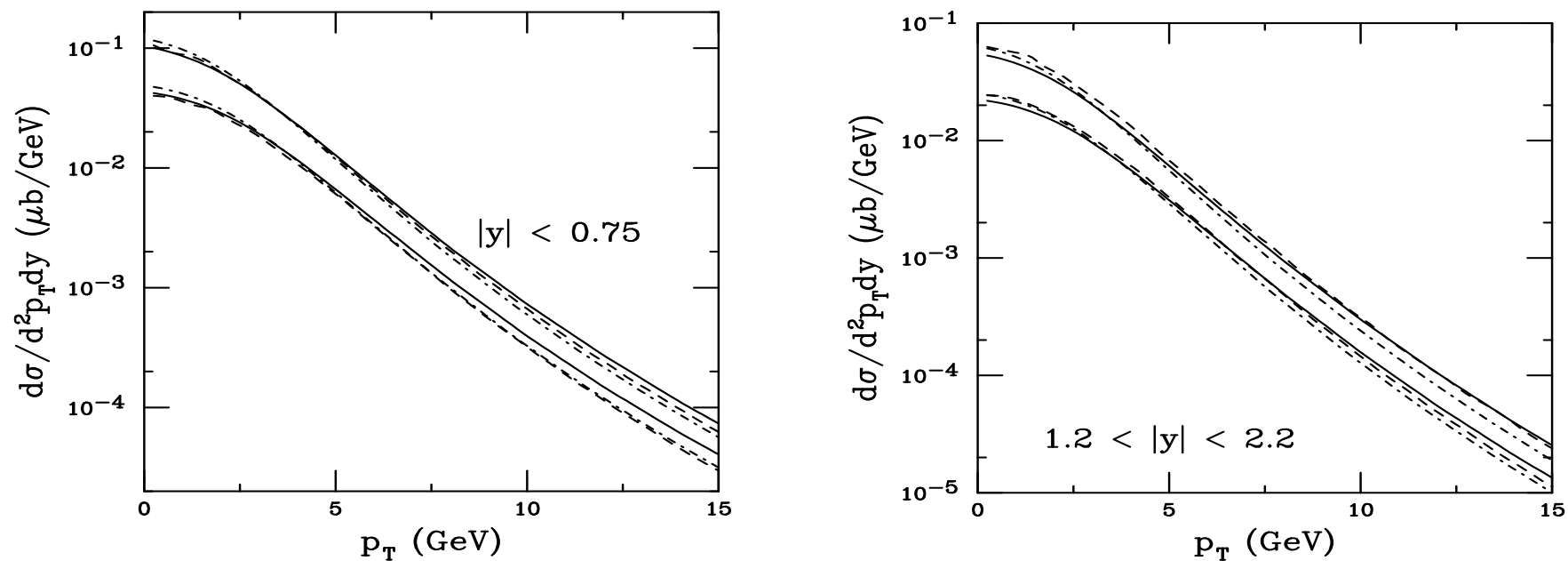


Figure 18: The bottom quark theoretical band as a function of p_T for FONLL (solid curves) and NLO (dashed curves) in $\sqrt{s} = 500$ GeV pp collisions. Also shown is the B meson uncertainty band, all using the CTEQ6M parton densities. The left-hand plot gives the result for $|y| \leq 0.75$ while the right-hand plot shows the result for $1.2 \leq |y| \leq 2.2$.

Uncertainty Bands for Electrons from Heavy Flavor Decays at 200 GeV

Electrons from B decays begin to dominate at $p_T \sim 5$ GeV

Electron spectra very sensitive to rapidity range – to get $|y| \leq 0.75$ electrons, need $|y| \leq 2$ charm and bottom range

Forward electron spectra thus not possible to obtain using FONLL code due to problems at large y

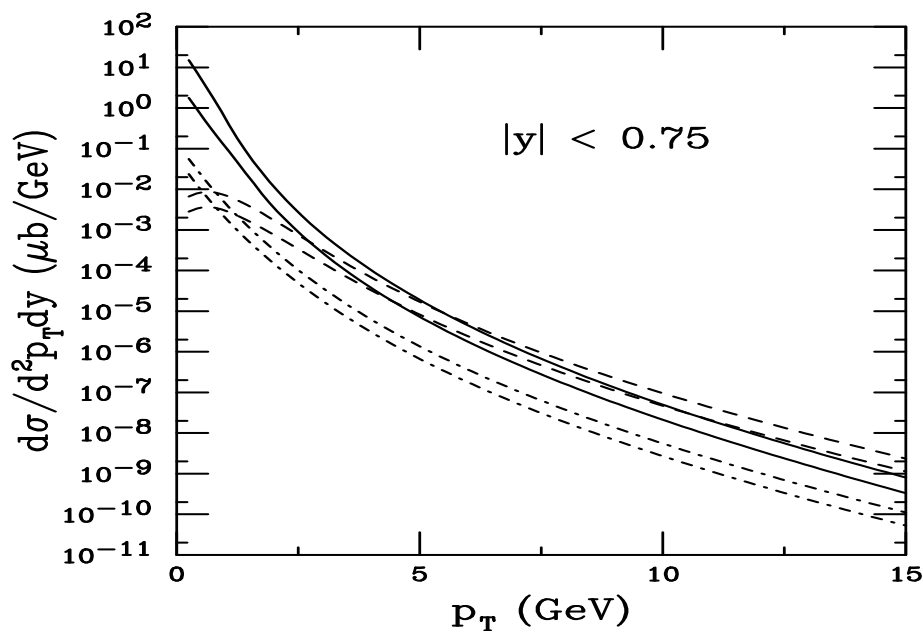


Figure 19: The theoretical FONLL bands for $D \rightarrow eX$ (solid), $B \rightarrow eX$ (dashed) and $B \rightarrow DX \rightarrow eX'$ (dot-dashed) as a function of p_T in $\sqrt{s} = 200$ GeV pp collisions for $|y| < 0.75$.

Uncertainty Bands for Electrons from Heavy Flavor Decays at 500 GeV

Crossover between B and D dominance is similar at the higher energy

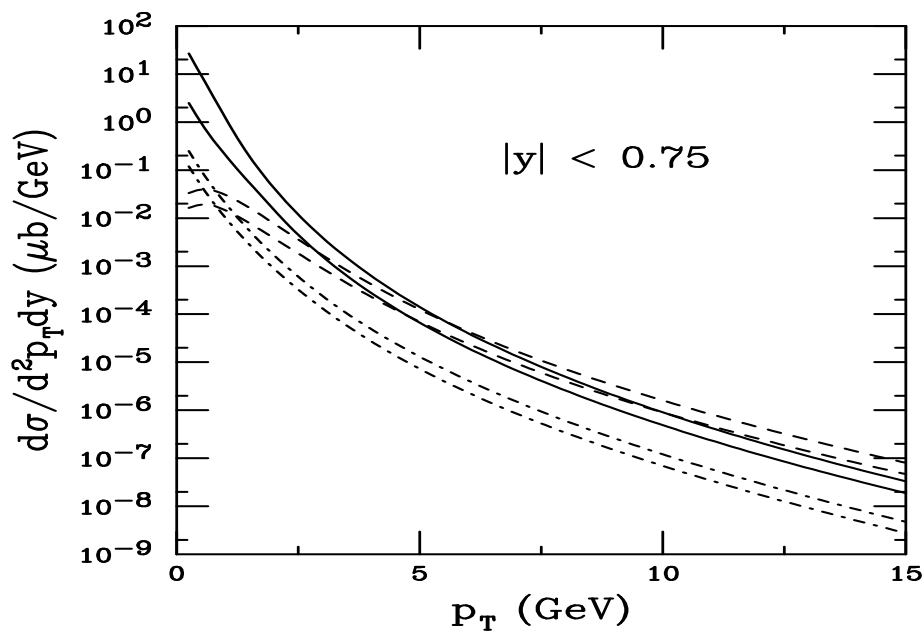


Figure 20: The theoretical FONLL bands for $D \rightarrow eX$ (solid), $B \rightarrow eX$ (dashed) and $B \rightarrow DX \rightarrow eX'$ (dot-dashed) as a function of p_T in $\sqrt{s} = 500$ GeV pp collisions for $|y| < 0.75$.

Charm Cross Sections

m (GeV)	μ_F/m_T	μ_R/m_T	$\sigma(\text{all } y)$ (μb)	$\sigma(y \leq 0.75)$ (μb)	$\sigma(1.2 \leq y \leq 2.2)$ (μb)
$\sqrt{s} = 200$ GeV					
1.3	1	1	367.4	130.9	54.75
1.5	1	1	234.2	85.69	34.70
1.7	1	1	151.2	56.71	22.32
1.5	0.5	0.5	368.8	118.5	56.93
1.5	0.5	1	110.3	38.18	16.65
1.5	1	0.5	649.4	231.0	97.21
1.5	2	2	180.4	66.15	26.77
1.5	2	1	317.5	114.9	47.20
1.5	1	2	129.4	47.74	19.12
$\sqrt{s} = 500$ GeV					
1.3	1	1	749.8	216.0	190.9
1.5	1	1	531.6	157.9	78.67
1.7	1	1	376.3	115.1	55.95
1.5	0.5	0.5	657.0	156.2	96.41
1.5	0.5	1	203.7	54.33	30.03
1.5	1	0.5	1448	413.0	214.4
1.5	2	2	490.9	147.1	72.71
1.5	2	1	823.5	242.3	121.3
1.5	1	2	294.7	88.66	43.57

Table 3: Charm cross sections obtained from the parameter sets used to determine the theoretical uncertainty band in pp collisions at $\sqrt{s} = 200$ and 500 GeV with the CTEQ6M densities.

Bottom Cross Sections

m (GeV)	μ_F/m	μ_R/m	$\sigma(\text{all } y)$ (μb)	$\sigma(y \leq 0.75)$ (μb)	$\sigma(1.2 \leq y \leq 2.2)$ (μb)
$\sqrt{s} = 200$ GeV					
4.5	1	1	2.38	1.100	0.320
4.75	1	1	1.82	0.846	0.242
5	1	1	1.40	0.661	0.185
4.75	0.5	0.5	2.72	1.253	0.365
4.75	0.5	1	1.87	0.864	0.249
4.75	1	0.5	2.67	1.236	0.357
4.75	2	2	1.25	0.589	0.166
4.75	2	1	1.74	0.814	0.231
4.75	1	2	1.33	0.621	0.176
$\sqrt{s} = 500$ GeV					
4.5	1	1	12.26	4.69	1.81
4.75	1	1	9.77	3.78	1.44
5	1	1	7.87	3.08	1.16
4.75	0.5	0.5	13.51	5.19	1.99
4.75	0.5	1	8.98	3.47	1.38
4.75	1	0.5	14.29	5.50	2.11
4.75	2	2	7.40	2.88	1.09
4.75	2	1	10.09	3.91	1.49
4.75	1	2	7.16	2.78	1.05

Table 4: Bottom cross sections obtained from the parameter sets used to determined the theoretical uncertainty band in pp collisions at $\sqrt{s} = 200$ and 500 GeV with the CTEQ6M densities.

A Dependence

To estimate the effects of nuclear shadowing, it is not feasible to make ratios from the uncertainty bands: since the bands contain an admixture of curves, they are affected differently by shadowing than the comparison of results in pp , pA and AA with the same parameters

In any case, the p_T distributions are not very useful as a measure of shadowing since the rapidity-integrated effect is on the order of 10-15%

Better to look at p_T -integrated rapidity distributions, if possible

Comparison of NLO Charm Rapidity Distributions

pA rapidity distributions skewed toward negative rapidity due to shadowing at large rapidity

pp distributions broader at 500 GeV

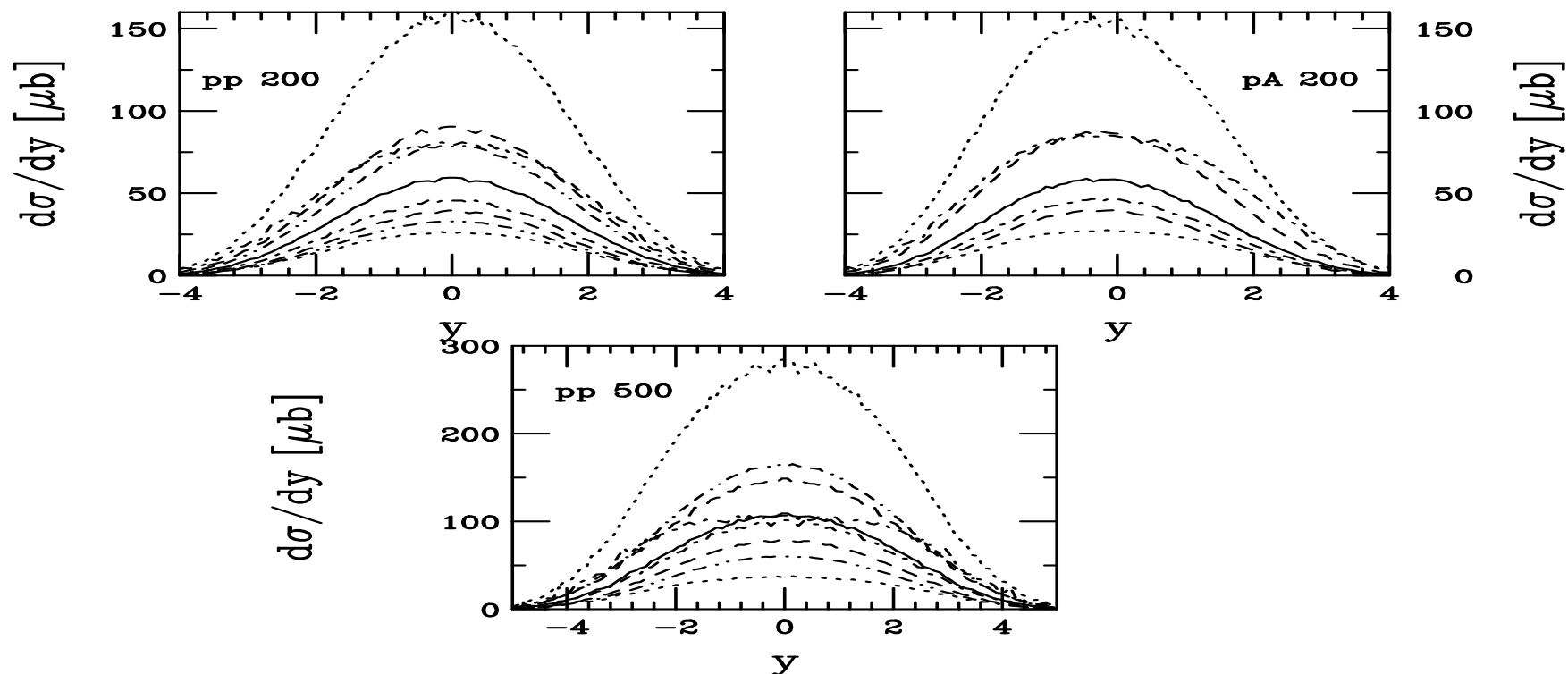


Figure 21: The charm quark rapidity distributions calculated using CTEQ6M. The solid curve is the central value $(\mu_F/m_T, \mu_R/m_T) = (1, 1)$ with $m = 1.5$ GeV. The upper and lower dashed curves are $m = 1.3$ and 1.7 GeV with $(1, 1)$ respectively. The upper and lower dot-dashed curves correspond to $(0.5, 0.5)$ and $(2, 2)$ while the upper and lower dotted curves are with $(1, 0.5)$ and $(0.5, 1)$ with $m = 1.5$ GeV and the upper and lower dot-dot-dot-dashed curves are with $(2, 1)$ and $(1, 2)$.

Comparison of NLO Bottom Rapidity Distributions

pp distributions broader at 500 GeV

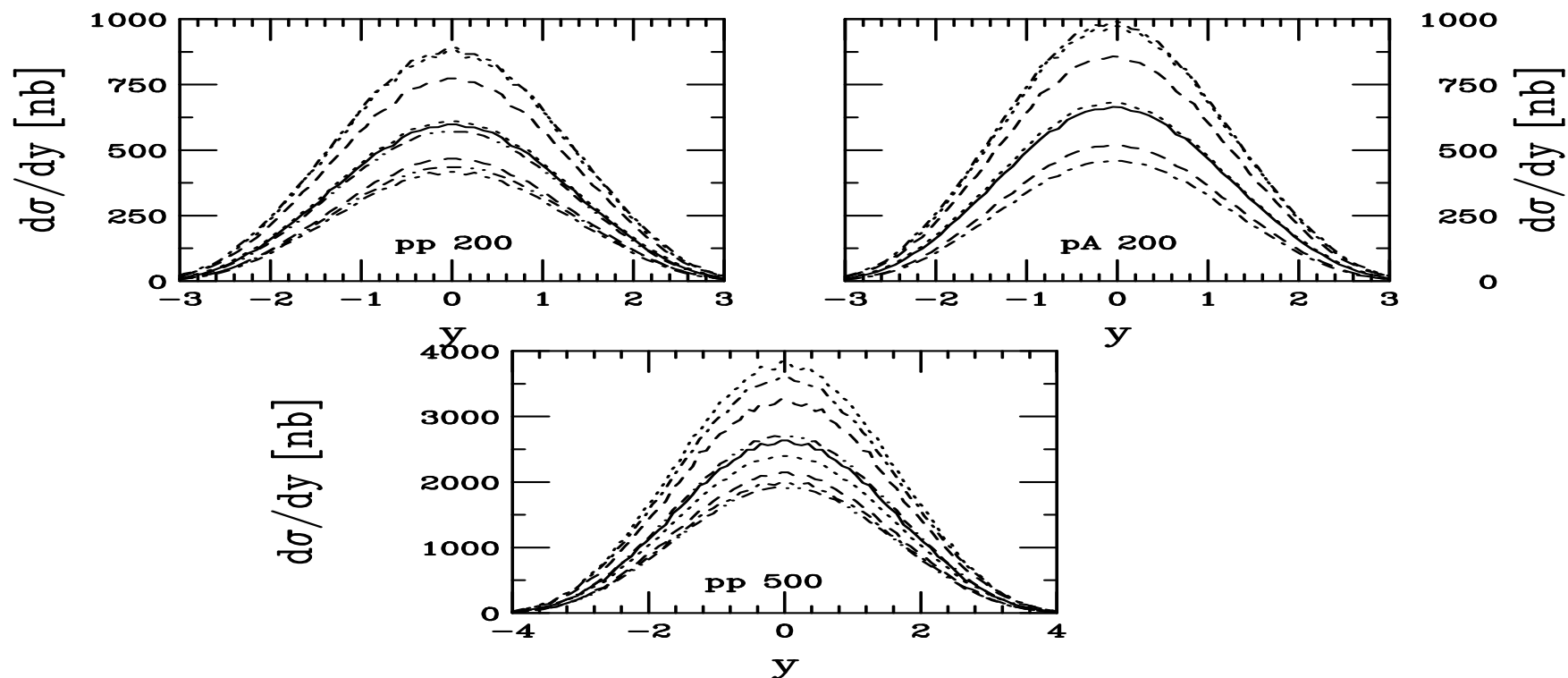


Figure 22: The bottom quark rapidity distributions calculated using CTEQ6M. The solid curve is the central value $(\mu_F/m_T, \mu_R/m_T) = (1, 1)$ with $m = 4.75$ GeV. The upper and lower dashed curves are $m = 4.5$ and 5 GeV with $(1, 1)$ respectively. The upper and lower dot-dashed curves correspond to $(0.5, 0.5)$ and $(2, 2)$ while the upper and lower dotted curves are with $(1, 0.5)$ and $(0.5, 1)$ with $m = 4.75$ GeV and the upper and lower dot-dot-dot-dashed curves are with $(2, 1)$ and $(1, 2)$.

Quarkonium Production: Color Evaporation Model (CEM)

Gavai *et al.*, G. Schuler and R.V.

All quarkonium states are treated like $Q\bar{Q}$ below $H\bar{H}$ threshold

Distributions (x_F, p_T, \sqrt{s}, A) for all quarkonium family members identical — leads to constant ratios

At LO, $gg \rightarrow Q\bar{Q}$ and $q\bar{q} \rightarrow Q\bar{Q}$; NLO add $gq \rightarrow Q\bar{Q}q$

$$\sigma_C^{\text{CEM}} = F_C \sum_{i,j} \int_{4m^2}^{4m_H^2} d\hat{s} \int dx_1 dx_2 f_{i/p}(x_1, \mu^2) f_{j/p}(x_2, \mu^2) \hat{\sigma}_{ij}(\hat{s}) \delta(\hat{s} - x_1 x_2 s)$$

F_C fixed at NLO from total cross section data as a function of \sqrt{s} , $\sigma(x_F > 0)$ for inclusive J/ψ and $B_{\mu\mu} d\sigma(\Upsilon + \Upsilon' + \Upsilon'')_{y=0}/dy$

Values of m and μ (here $\mu \propto \sqrt{(p_{TQ}^2 + p_{T\bar{Q}}^2)/2 + m_Q^2} = m_{TQ\bar{Q}} \equiv m_T$ in the exclusive $Q\bar{Q}$ code) for several parton densities fixed from $Q\bar{Q}$ production (Method 1)

Production and Feeddown Fractions

Data and branching ratios can be used to separate out the F_C 's for each state in quarkonium family

Resonance	$\sigma_i^{\text{dir}}/\sigma_H$	f_i
J/ψ	0.62	0.62
ψ'	0.14	0.08
χ_{c1}	0.6	0.16
χ_{c2}	0.99	0.14
Υ	0.52	0.52
Υ'	0.33	0.10
Υ''	0.20	0.02
$\chi_b(1P)$	1.08	0.26
$\chi_b(2P)$	0.84	0.10

Table 5: The ratios of the direct quarkonium production cross sections, σ_i^{dir} , to the inclusive J/ψ and Υ cross sections, denoted σ_H , and the feed down contributions of all states to the J/ψ and Υ cross sections, f_i .

Fitted Fractions and J/ψ Cross Sections in CEM

Case	PDF	m (GeV)	μ/m_T	$\sigma_{J/\psi}/\sigma_C^{\text{CEM}}$
ψ_1	MRST HO	1.2	2	0.0144
ψ_2	MRST HO	1.4	1	0.0248
ψ_3	CTEQ 5M	1.2	2	0.0155
ψ_4	GRV 98 HO	1.3	1	0.0229

Table 6: The production fractions obtained from simultaneously fitting F_C to the J/ψ total cross sections and $y = 0$ cross sections as a function of energy. The PDF, charm quark mass, and scales used are obtained from comparison of the $c\bar{c}$ cross section to data.

Case	$\sigma_{J/\psi}^{\text{inc}}$	$\sigma_{J/\psi}^{\text{dir}}$	$\sigma_{\chi_{c1}}$	$\sigma_{\chi_{c2}}$	$\sigma_{\psi'}$
ψ_1	2.35	1.46	1.41	2.33	0.33
ψ_2	1.76	1.09	1.06	1.74	0.25
ψ_3	2.84	1.76	1.70	2.81	0.40
ψ_4	2.10	1.31	1.26	2.08	0.29

Table 7: The charmonium cross sections (in μb) for 200 GeV pp collisions. The inclusive and direct J/ψ cross sections are both given.

Extrapolated J/ψ Total Cross Sections

Total forward J/ψ cross sections extrapolated to higher energy

Energy dependence obtained from NLO CEM

Factor of ~ 1.6 – 2 between results at 200 GeV and at 5.5 TeV

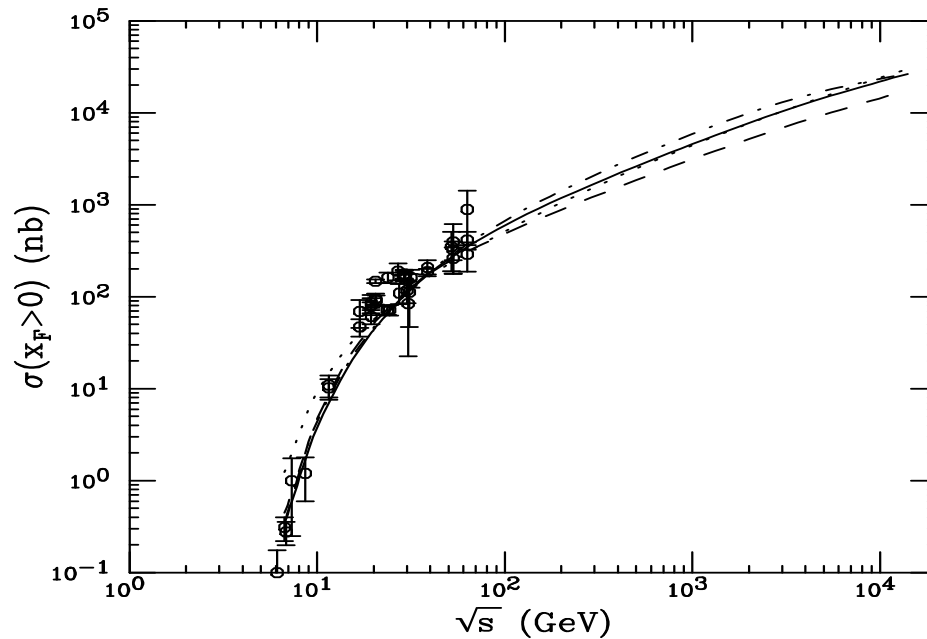


Figure 23: NLO J/ψ forward cross sections. The solid curve employs the MRST HO distributions with $m = 1.2$ GeV $\mu/m_T = 2$, the dashed, MRST HO with $m = 1.4$ GeV $\mu/m_T = 1$, the dot-dashed, CTEQ 5M with $m = 1.2$ GeV $\mu/m_T = 2$, and the dotted, GRV 98 HO with $m = 1.3$ GeV $\mu/m_T = 1$.

Fitted Fractions and Υ Cross Sections in CEM

Case	PDF	m (GeV)	μ/m_T	$\sigma_{B\Sigma\Upsilon}/\sigma_b^{\text{CEM}}$	$\sigma_{\Upsilon}/\sigma_b^{\text{CEM}}$
$\Upsilon 1$	MRST HO	4.75	1	0.000963	0.0276
$\Upsilon 2$	MRST HO	4.50	2	0.000701	0.0201
$\Upsilon 3$	MRST HO	5.00	0.5	0.001766	0.0508
$\Upsilon 4$	GRV 98 HO	4.75	1	0.000787	0.0225

Table 8: The production fractions obtained from fitting the CEM cross section to the combined Υ cross sections to muon pairs at $y = 0$ as a function of energy. The PDF, charm quark mass, and scales used are the same as those obtained by comparison of the $b\bar{b}$ cross section to data.

Case	σ_{Υ}	$\sigma_{\Upsilon'}$	$\sigma_{\Upsilon''}$	$\sigma_{\chi_b(1P)}$	$\sigma_{\chi_b(2P)}$
$\Upsilon 1$	3.43	2.18	1.32	7.13	5.54
$\Upsilon 2$	3.92	2.49	1.51	8.15	6.34
$\Upsilon 3$	2.99	1.90	1.15	6.21	4.83
$\Upsilon 4$	2.24	1.42	0.86	4.66	3.62

Table 9: The direct bottomonium cross sections (in nb) for pp collisions at 200 GeV. The production fractions for the total Υ are multiplied by the appropriate ratios determined from data.

Inclusive Υ Cross Sections at $y = 0$

Cross sections include all $\Upsilon(nS)$ states and their decays to muon pairs

Data is from pp interactions except for highest two points where only $p\bar{p}$ colliders available

At high energies, $gg \rightarrow Q\bar{Q}$ dominates and differences between $p\bar{p} \rightarrow \Upsilon$ and $pp \rightarrow \Upsilon$ are negligible

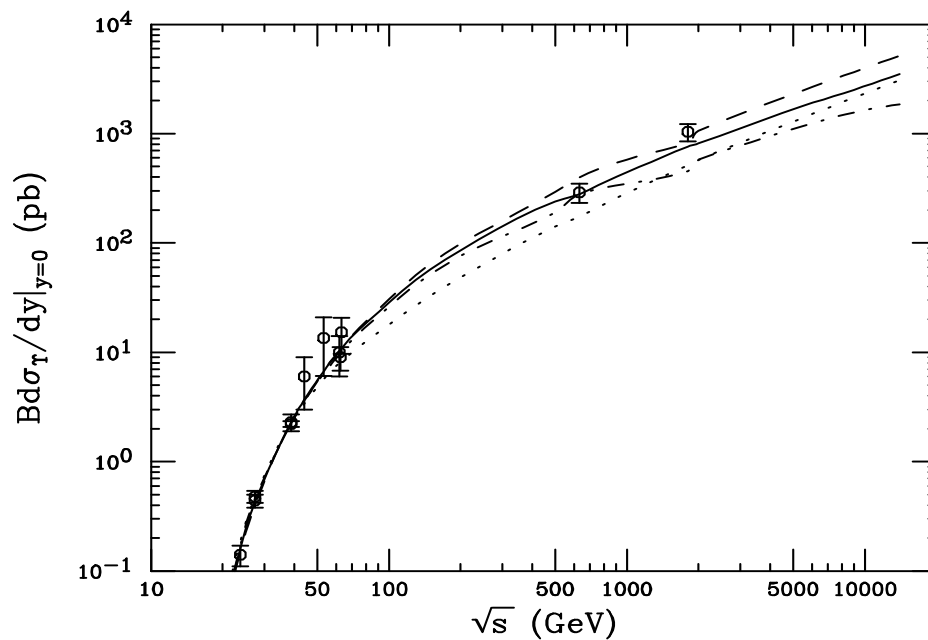


Figure 24: Inclusive Υ production data, combined from all three S states, and compared to NLO CEM calculations. The solid curve employs the MRST HO distributions with $m = 4.75$ GeV $\mu/m_T = 1$, the dashed, $m = 4.5$ GeV $\mu/m_T = 0.5$, the dot-dashed, $m = 5$ GeV $\mu/m_T = 2$, and the dotted, GRV 98 HO with $m = 4.75$ GeV $\mu/m_T = 1$.

The Quarkonium p_T Distribution in the $Q\bar{Q}$ NLO Code

Gaussian k_T smearing, $\langle k_T^2 \rangle_p = 1 \text{ GeV}^2$ for fixed target pp and πp , broadened for pA and AA , NLO code adds in final state:

$$g_p(k_T) = \frac{1}{\pi \langle k_T^2 \rangle_p} \exp(-k_T^2 / \langle k_T^2 \rangle_p)$$

Comparison with J/ψ and Υ Tevatron data at 1.8 TeV shows that the broadening should increase with energy, to $\langle k_T^2 \rangle_p \approx 2.5 \text{ GeV}^2$

Fits of increase of $\langle p_T^2 \rangle$ to old data are inadequate to explain this increase so we make a simple linear extrapolation to obtain

$$\langle k_T^2 \rangle_p = 1 + \frac{1}{6} \ln \left(\frac{s}{s_0} \right) \text{ GeV}^2$$

Thus at RHIC energies $\langle k_T^2 \rangle_p = 1.77 \text{ GeV}^2$ for 200 GeV and 2.07 GeV^2 for 500 GeV pp collisions

Comparison with Tevatron J/ψ p_T Distributions

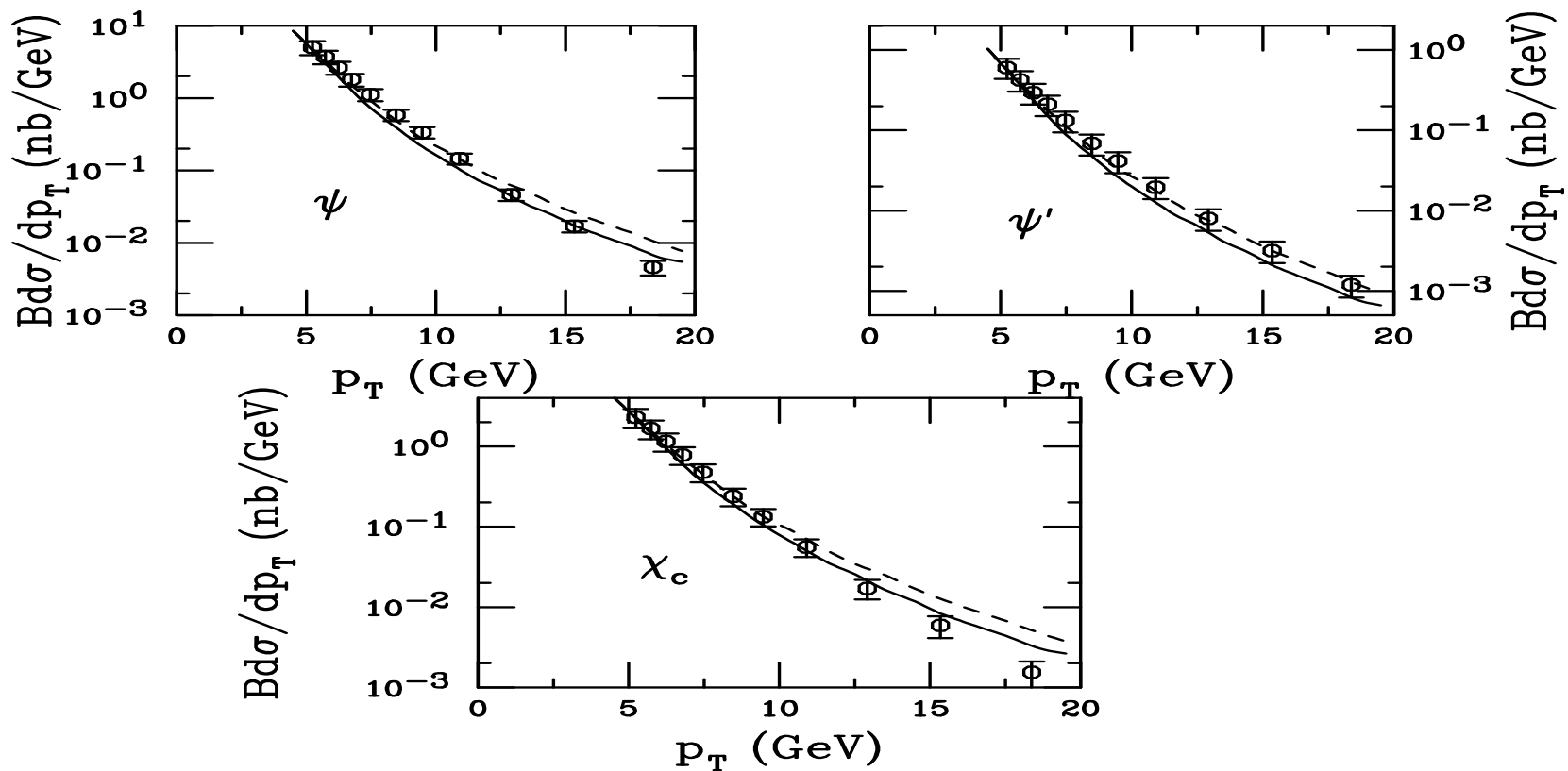


Figure 25: The p_T distributions of direct J/ψ as well as J/ψ 's from ψ' and χ_c decays calculated for cases ψ_1 (solid) and ψ_4 (dashed) are compared to the CDF data. We use $\langle k_T^2 \rangle_p = 2.5 \text{ GeV}^2$.

Comparison with Tevatron Υ p_T Distributions

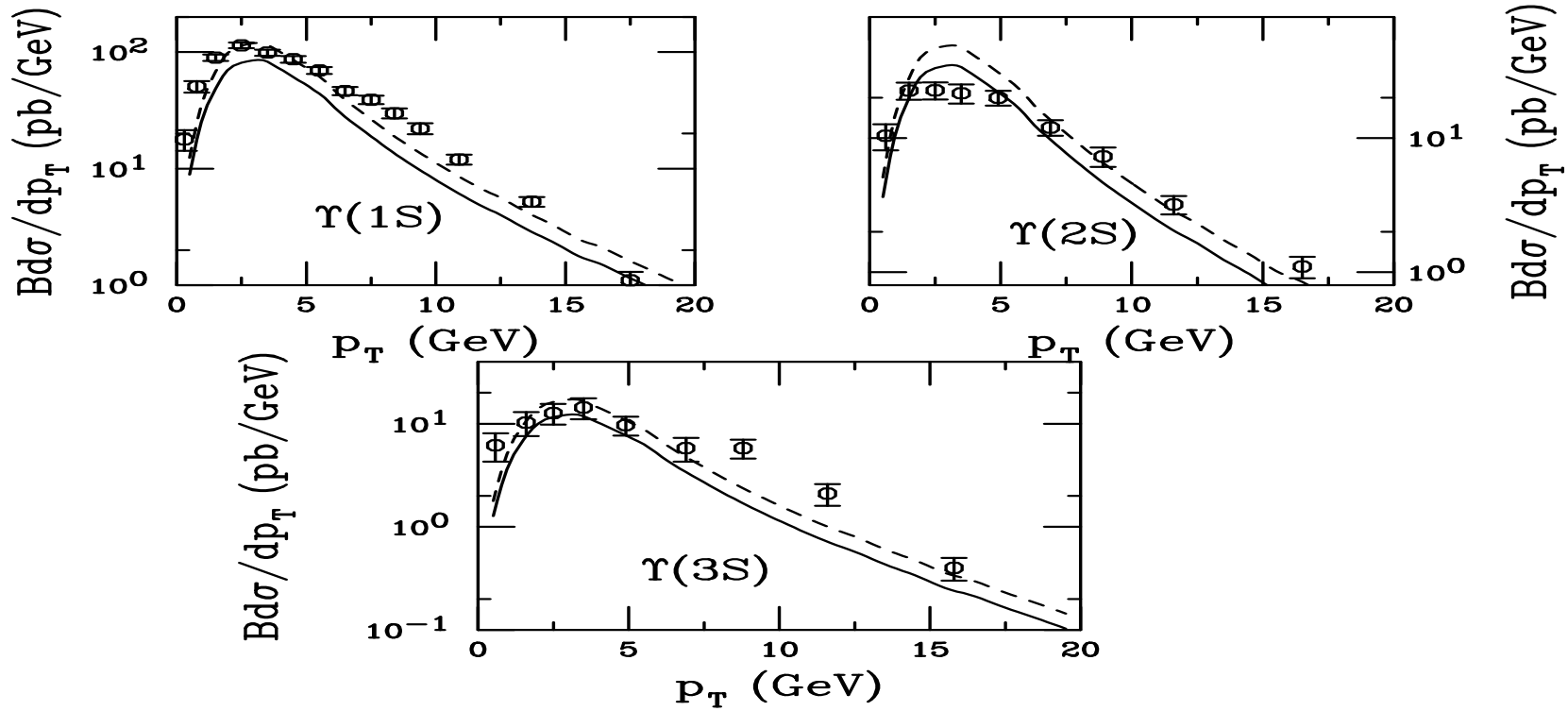


Figure 26: The p_T distributions of inclusive $\Upsilon(1S)$, $\Upsilon(2S)$ and $\Upsilon(3S)$ calculated for case $\Upsilon 1$ with $\langle k_T^2 \rangle_p = 3 \text{ GeV}^2$ are compared to the CDF data. The dashed curve is multiplied by a K factor of 1.4.

Nuclear Effects on p_T Broadening

Additional broadening – beyond the intrinsic broadening – assumed to arise from multiple parton scattering in the target before hard interaction

J/ψ , Υ and Drell-Yan show effects of broadening in pA , parameterized as

$$\langle k_T^2 \rangle_{iA} = \langle k_T^2 \rangle_p + (\langle \nu \rangle - 1) \Delta^2(\mu)$$

The broadening is proportional to the average number of collisions of the projectile parton in the target,

$$\langle \nu \rangle = \sigma_{NN} \frac{\int d^2b T_A^2(b)}{\int d^2b T_A(b)} = \frac{3}{2} \sigma_{NN} \rho_0 R_A$$

$T_A(b)$ is the nuclear profile function

The second equality is average over impact parameter assuming a spherical nucleus, $\rho_0 = 0.16 \text{ fm}^{-3}$ is the central nuclear density and R_A is the nuclear radius

$\Delta^2(\mu = 2m)$, the strength of the broadening, depends on the scale of the interactions

$$\Delta^2(\mu) = 0.225 \frac{\ln^2(\mu/\text{GeV})}{1 + \ln(\mu/\text{GeV})} \text{GeV}^2$$

	$\frac{(\langle \nu \rangle - 1) \Delta^2(\mu) \text{ (GeV}^2\text{)}}{Q\bar{Q}}$	$\frac{(\langle \nu \rangle - 1) \Delta^2(\mu) \text{ (GeV}^2\text{)}}{pA \text{ central } AA}$
$c\bar{c}$	0.35	0.7
$b\bar{b}$	1.57	3.14

Prediction of J/ψ p_T Distributions at RHIC II

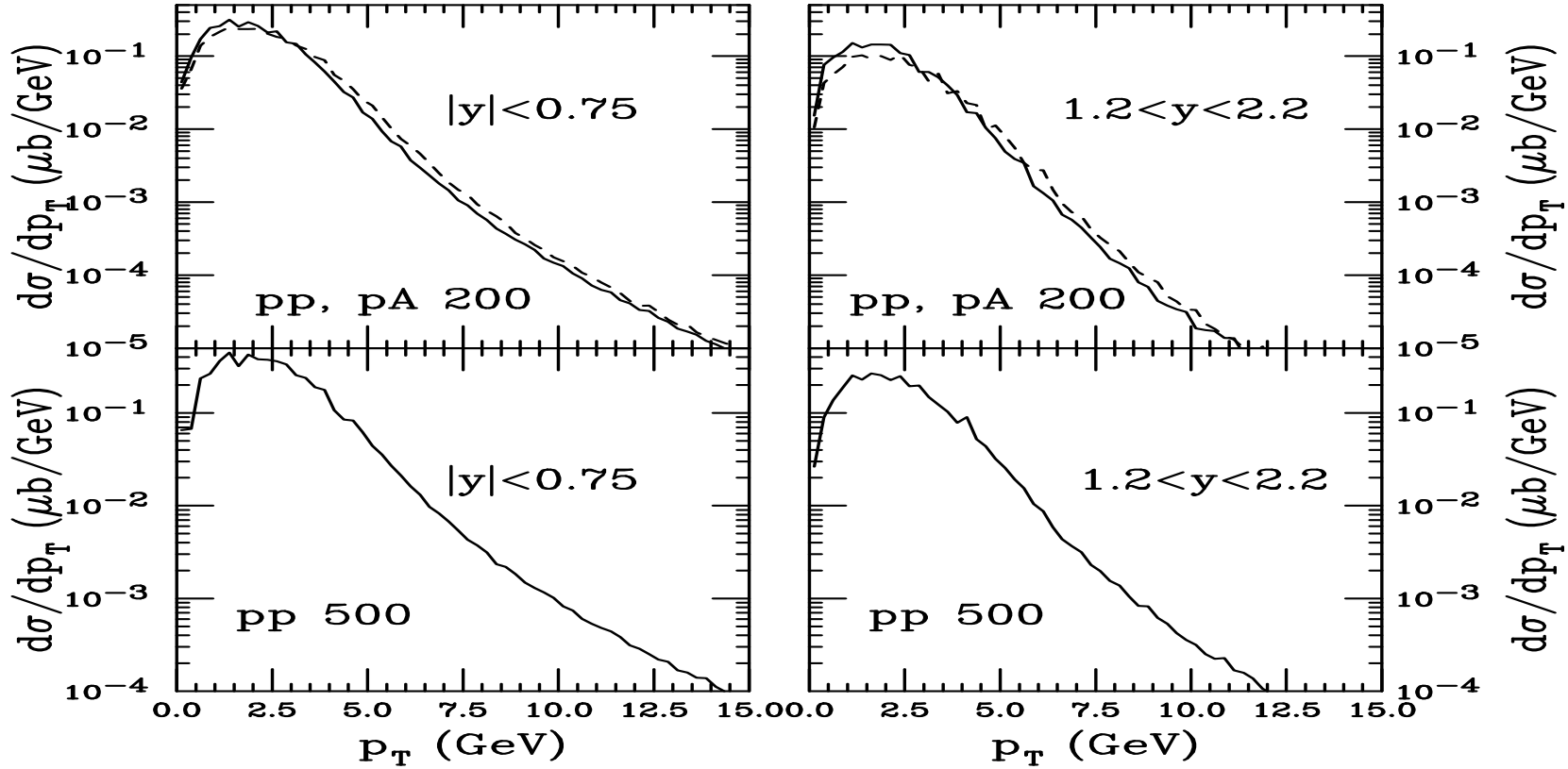


Figure 27: The inclusive J/ψ p_T distributions at $\sqrt{s} = 200$ and 500 GeV using case $\psi 1$ (solid). We use $\langle k_T^2 \rangle_p = 1.77 \text{ GeV}^2$ for pp collisions and include broadening in pA collisions (dashed).

Prediction of J/ψ Rapidity Distributions at RHIC II

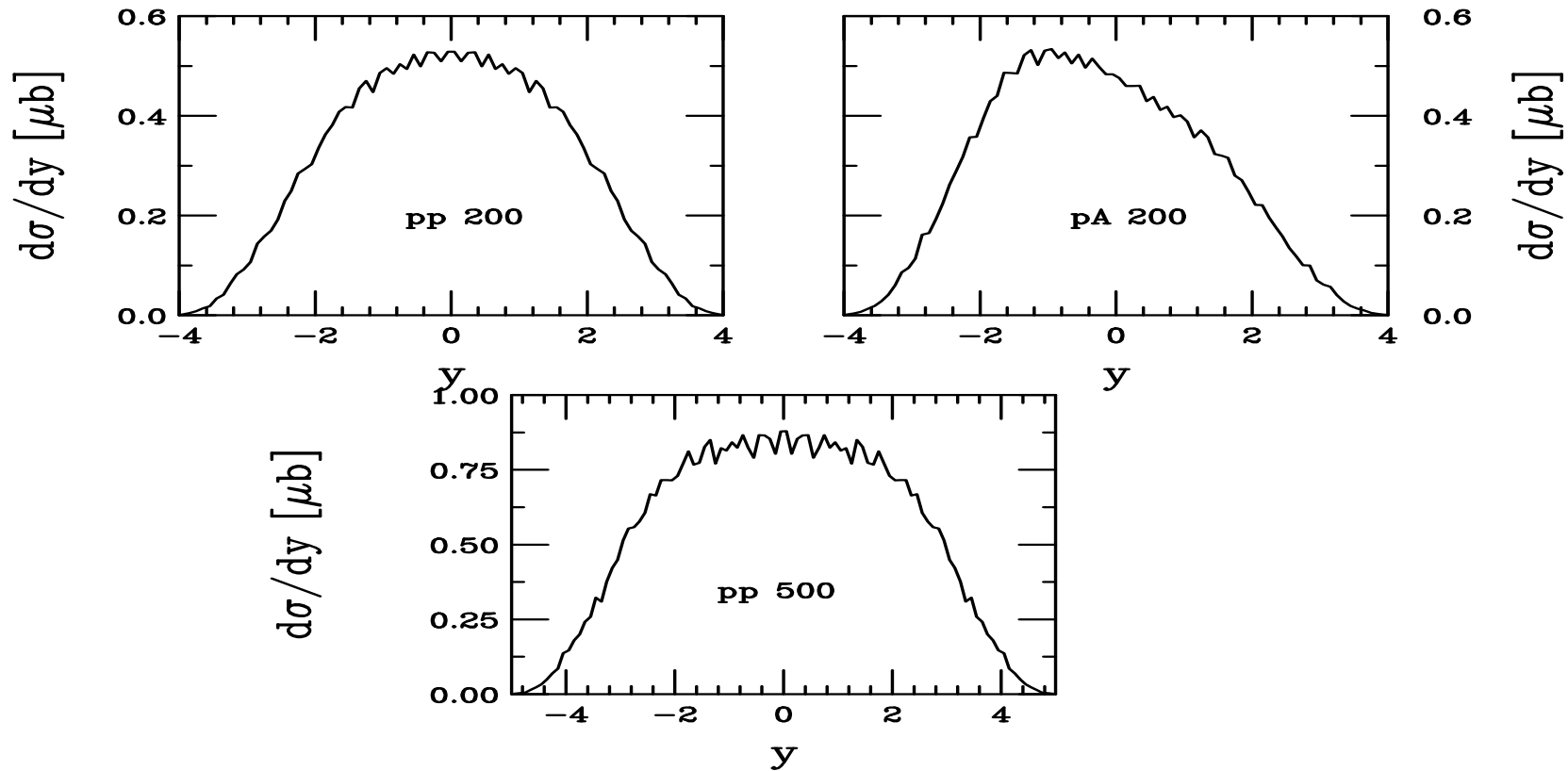


Figure 28: The inclusive J/ψ y distributions at $\sqrt{s} = 200$ and 500 GeV using case $\psi 1$ (solid). The rapidity distribution is unaffected by broadening.

Prediction of Υ p_T Distributions at RHIC II

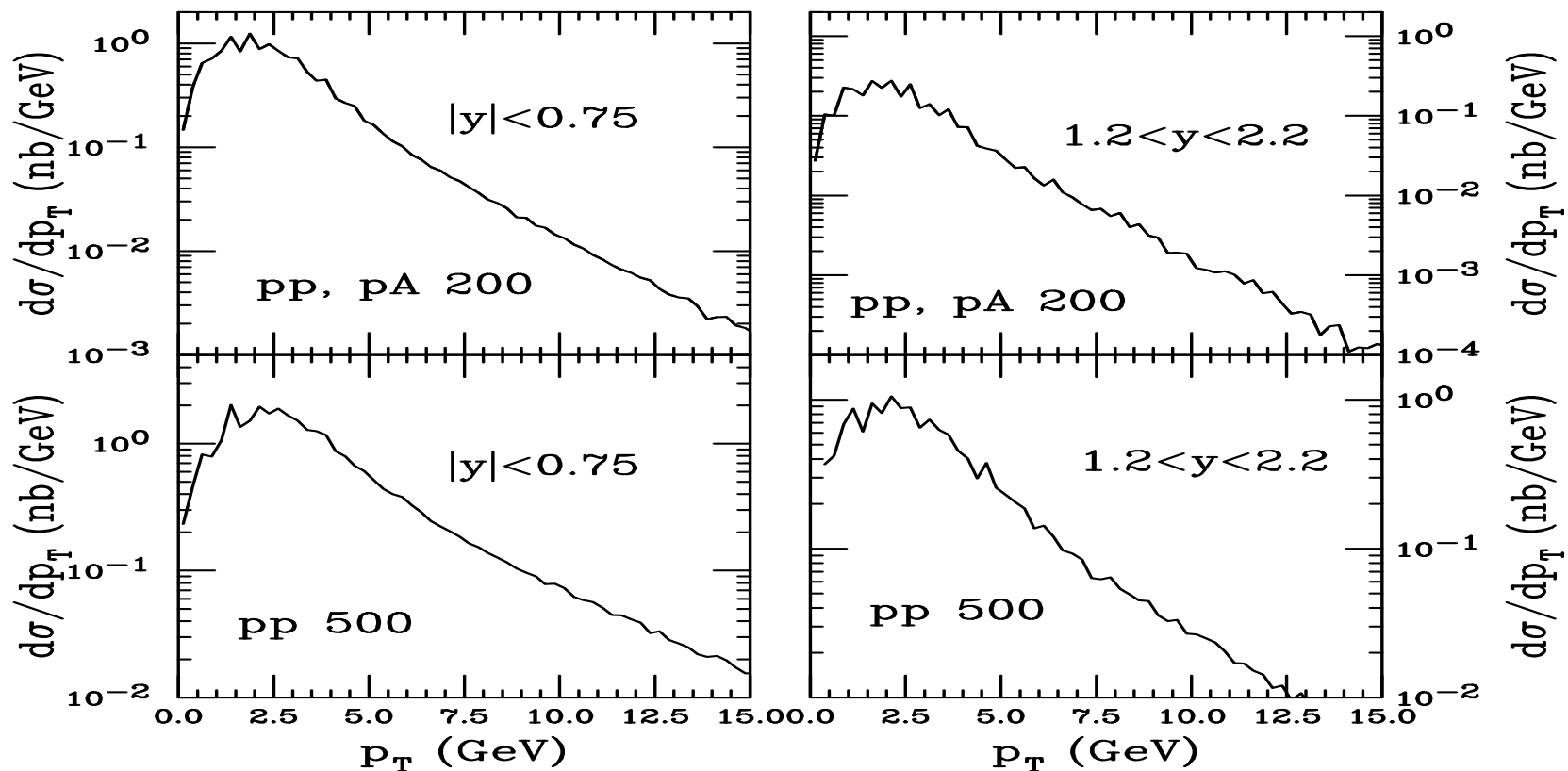


Figure 29: The inclusive Υ p_T distributions at $\sqrt{s} = 200$ and 500 GeV using case $\Upsilon 1$. We use $\langle k_T^2 \rangle_p = 1.77$ GeV² for pp collisions.

Prediction of Υ Rapidity Distributions at RHIC II

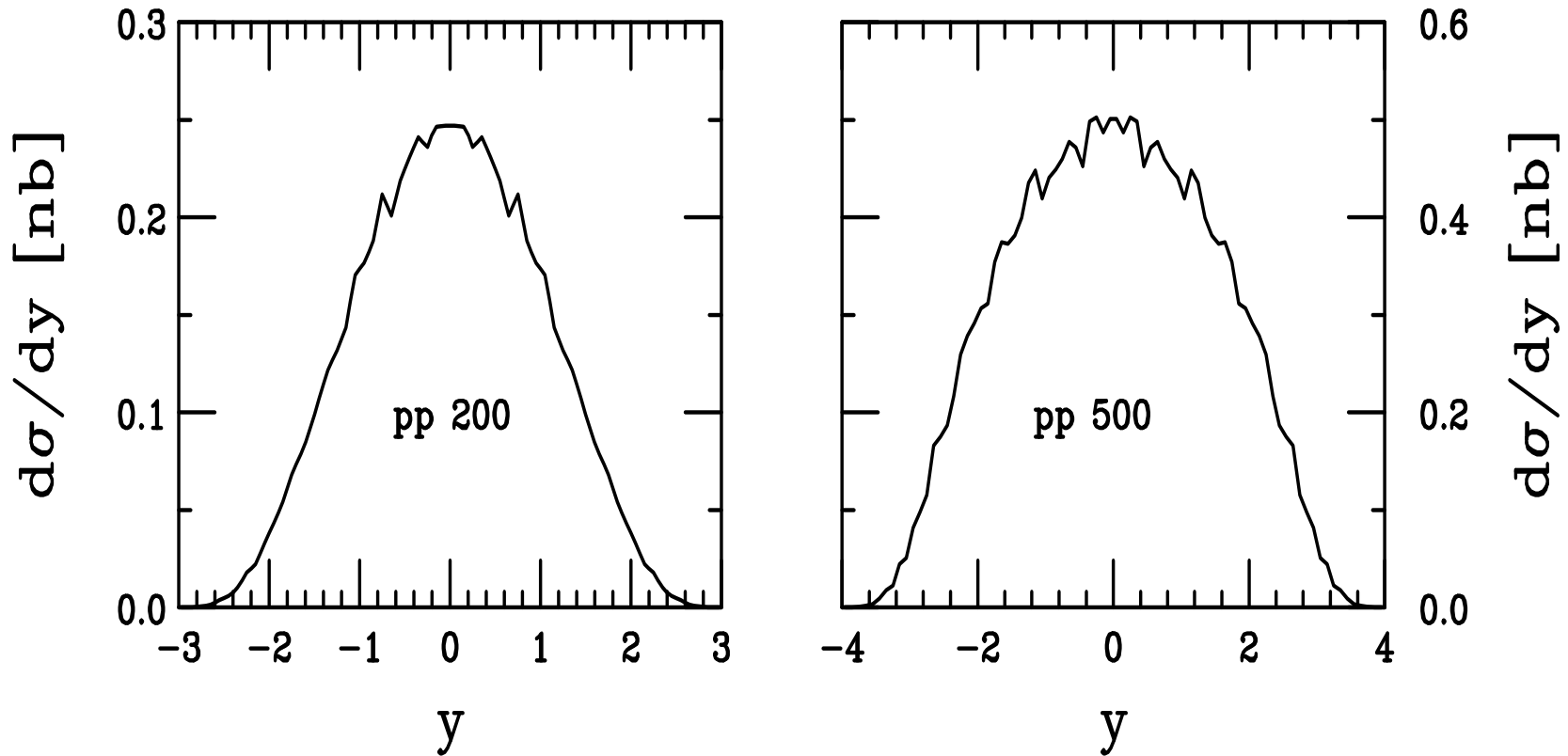


Figure 30: The inclusive Υ y distributions at $\sqrt{s} = 200$ and 500 GeV for case $\Upsilon 1$.

In dA Interactions, Nuclear Effects on Rapidity Distributions Become Important

Nuclear effects seen to be important in charmonium production at fixed target energies

In extrapolated pA cross sections, the exponent α was shown to be a function of both x_F and p_T

Several mechanisms affect A dependence in cold matter, we consider two here:

- Nuclear Shadowing — initial-state effect on the parton distributions affecting the level of production, important as a function of rapidity/ x_F
- Absorption — final-state effect, after $c\bar{c}$ that forms the J/ψ has been produced, pair breaks up in matter due to interactions with nucleons

Here we only show effects on charmonium, Υ studies not done yet

Nuclear Parton Distributions

Nuclear parton densities

$$F_i^A(x, Q^2, \vec{r}, z) = \rho_A(s) S^i(A, x, Q^2, \vec{r}, z) f_i^N(x, Q^2) s = \sqrt{b^2 + z^2}$$

$$\rho_A(s) = \rho_0 \frac{1 + \omega(s/R_A)^2}{1 + \exp[(s - R_A)/d]}$$

We use EKS98 and Frankfurt, Guzey and Strikman (FGS) parameterizations: original, FGSo, high, FGSh, and low, FGS1, gluon shadowing

EKS98 has no spatial dependence, two FGS inhomogeneous parameterization recently made available — compare our spatial parameterizations with those of FGS

With no nuclear modifications, $S^i(A, x, Q^2, \vec{r}, z) \equiv 1$.

Spatial dependence of shadowing

Proportional to local nuclear density:

$$S_{\text{WS}}^i = S^i(A, x, Q^2, \vec{r}, z) = 1 + N_{\text{WS}}[S^i(A, x, Q^2) - 1] \frac{\rho(s)}{\rho_0}$$

Proportional to nuclear path length:

$$S_\rho^i(A, x, Q^2, \vec{r}, z) = 1 + N_\rho[S^i(A, x, Q^2) - 1] \frac{\int dz \rho_A(\vec{r}, z)}{\int dz \rho_A(0, z)}.$$

Normalization: $(1/A) \int d^2r dz \rho_A(s) S_{\text{WS}, \rho}^i \equiv S^i$. Larger than average modifications for $b = 0$. Nucleons like free protons when $s \gg R_A$. Similar normalization for FGS inhomogeneous parameterizations.

Comparing Shadowing Parameterizations: x Dependence

Recent parameterizations by Frankfurt *et al* use EKS98 for valence shadowing, stronger gluon shadowing at low x , cuts off modification above $x = 0.25$ for sea, 0.03 for gluon

Newer FGS parameterizations have lower gluon antishadowing, smoother x dependence over $10^{-4} < x < 0.02$

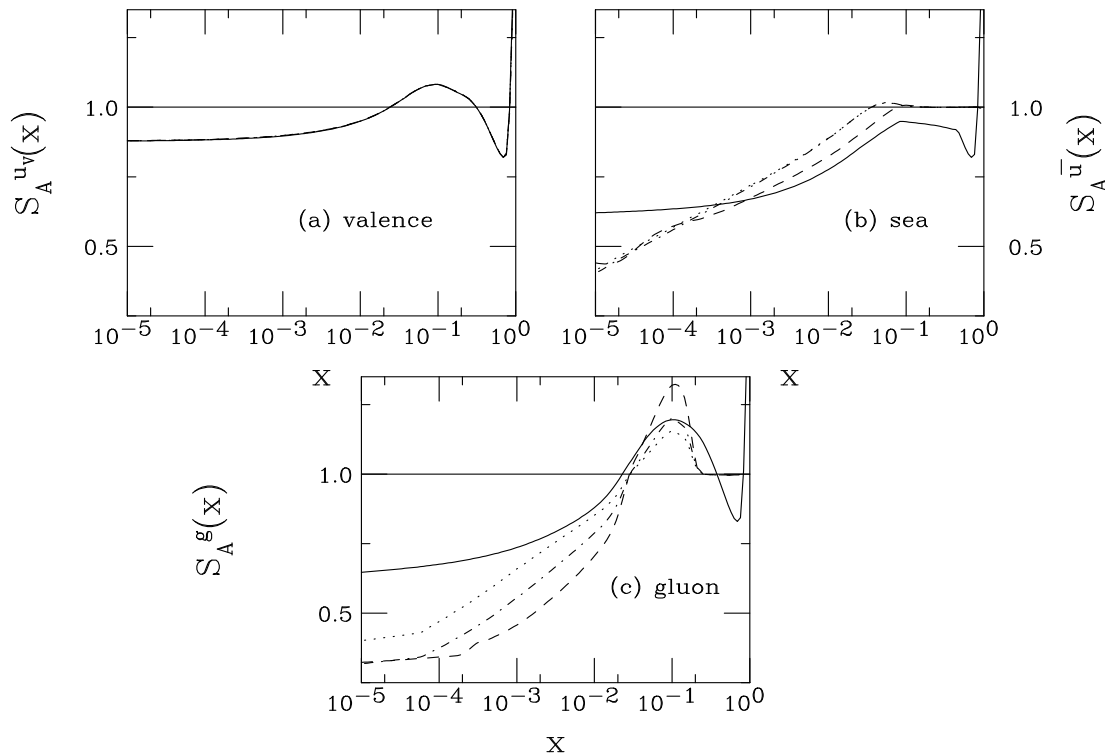


Figure 31: The EKS98 and FGS shadowing parameterizations are compared at the scale $\mu = 2m = 2.4$ GeV. The solid curves are the EKS98 parameterization, the dashed, FGS_o, dot-dashed, FGS_h, dotted, FGS_l.

Average x_2 as a Function of Energy and Rapidity

We calculate $\langle x_2 \rangle$ as a function of rapidity in the CEM (N.B. $\langle x_1 \rangle$ is mirror image of $\langle x_2 \rangle$)

Increasing \sqrt{S} broadens y range and decreases x_2

In PHENIX muon arms, it is possible to reach lower $\langle x_2 \rangle$ than with leading hadrons at similar rapidities: gg dominates and scale is relatively lower

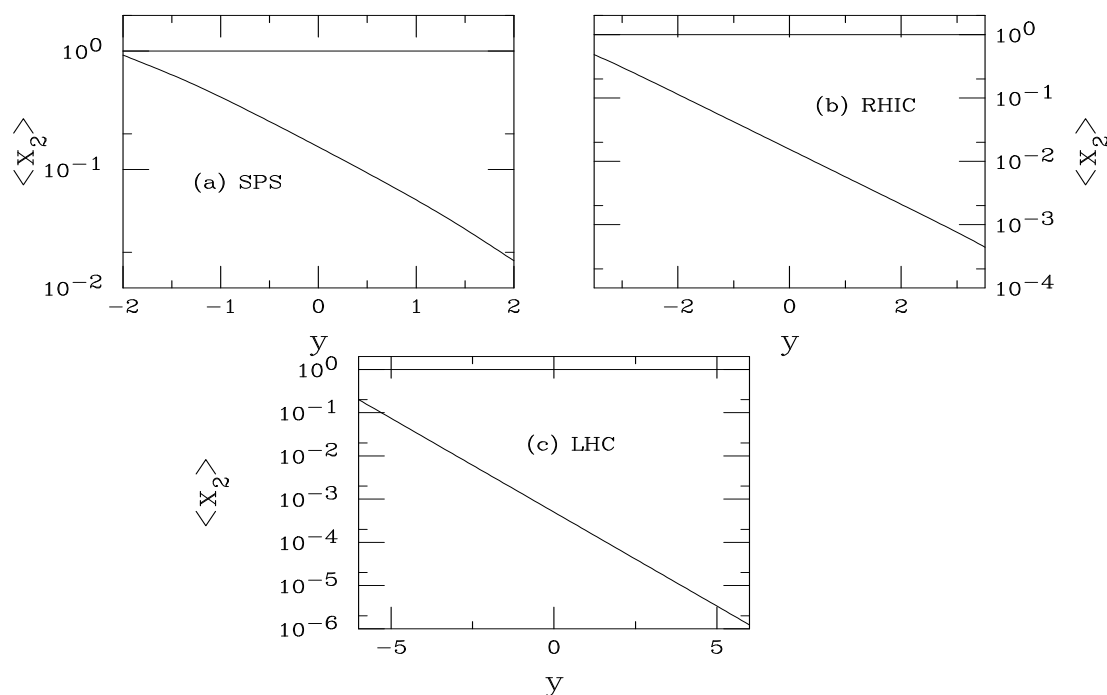


Figure 32: We give the average value of the nucleon momentum fraction, x_2 , in pp collisions as a function of rapidity for (a) the CERN SPS with $\sqrt{S} = 19.4$ GeV, (b) RHIC with $\sqrt{S} = 200$ GeV and (c) the LHC with $\sqrt{S} = 6.2$ TeV.

J/ψ Absorption by Nucleons

Woods-Saxon nuclear density profiles typically used

$$\begin{aligned}\sigma_{pA} &= \sigma_{pN} \int d^2b \int_{-\infty}^{\infty} dz \rho_A(b, z) S_A^{\text{abs}}(b) \\ &= \sigma_{pN} \int d^2b \int_{-\infty}^{\infty} dz \rho_A(b, z) \exp \left\{ - \int_z^{\infty} dz' \rho_A(b, z') \sigma_{\text{abs}}(z' - z) \right\}\end{aligned}$$

Note that if $\rho_A = \rho_0$, $\alpha = 1 - 9\sigma_{\text{abs}}/(16\pi r_0^2)$

Absorption models

singlet Individual charmonium cross sections grow quadratically with proper time until formation time; only effective when state can form in target

octet $|(c\bar{c})_8g\rangle$ state travels through nucleus, only forms charmonium outside; assume either “constant” over all y or “growing”, allowing octet to singlet conversion inside target at negative y – little difference at collider energy

NRQCD Nonrelativistic QCD approach differs from CEM in that states are produced with fixed singlet and octet contributions

We show results for absorption of color singlet and color octet states separately in the CEM and a combination of the two in NRQCD

Rapidity Dependence of Homogeneous Absorption

Results shown for different charmonium states: inclusive and direct J/ψ , ψ' and χ_c

Constant and growing octet indistinguishable in detector range, singlet absorption only effective for $y < -1$, NRQCD also shows little rapidity dependence

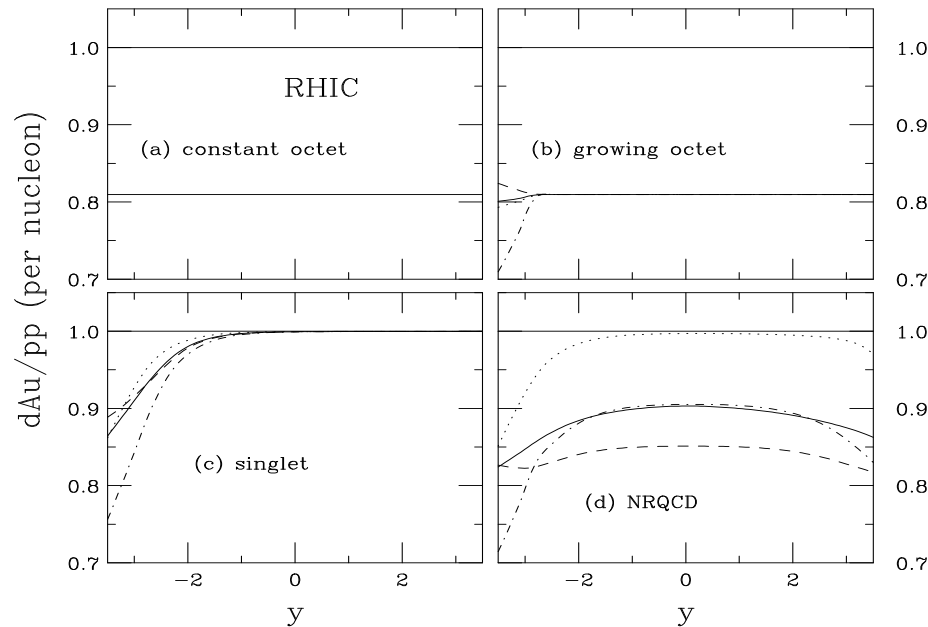


Figure 33: The J/ψ dAu/pp ratio at 200 GeV as a function of rapidity for absorption alone. We show (a) constant octet with 3 mb, (b) growing octet with 3 mb asymptotic cross section for all states, (c) singlet with 2.5 mb J/ψ absorption cross section, all calculated in the CEM and (d) NRQCD with a combination of octet and singlet matrix elements. The curves show total J/ψ (solid), direct J/ψ (dashed), ψ' (dot-dashed) and χ_c (dotted).

Effect of Inhomogeneous Absorption

Example of impact parameter dependence of absorption

Solid curve is 3 mb constant octet cross section, all rapidities, dashed is at $y = -2$, singlet

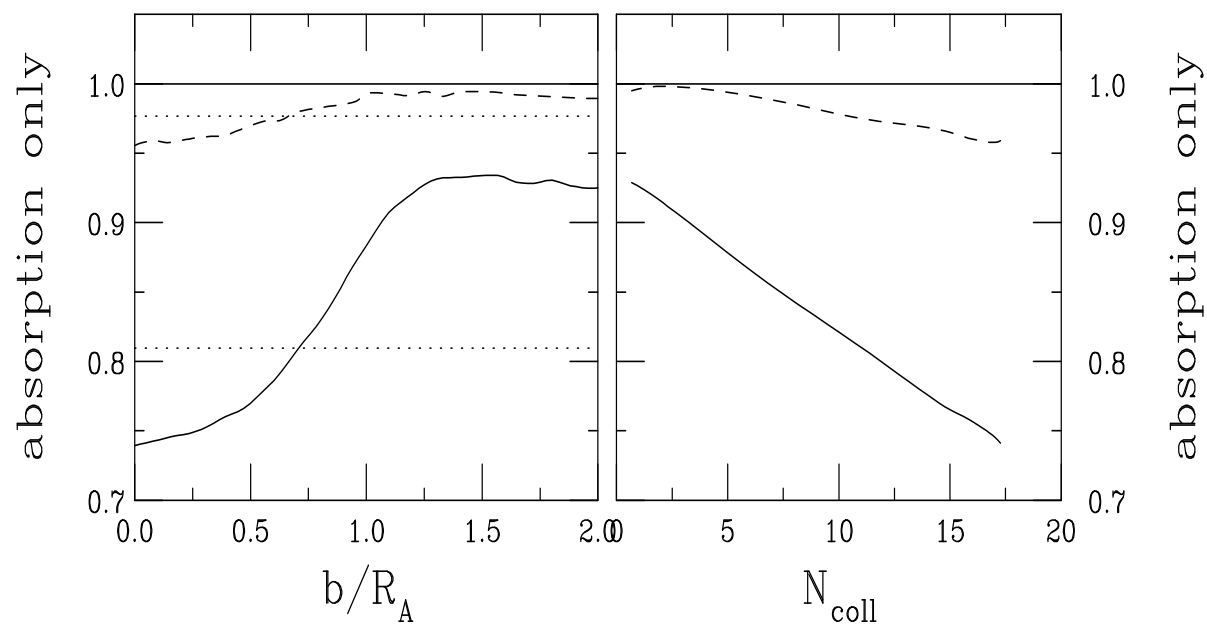


Figure 34: The J/ψ dAu/pp ratio as a function of b for absorption alone with $\sigma_{\text{abs}} = 3$ mb for a constant octet (all y), solid, and singlet ($y = -2$), dashed. The homogeneous results are indicated by the dotted lines.

Homogeneous Absorption and Shadowing at RHIC

Left-hand side: Effect of σ_{abs} is shown for various absorption models

Right-hand side: Comparing shadowing parameterizations for $\sigma_{\text{abs}} = 3$ mb, FGS1 similar to EKS98

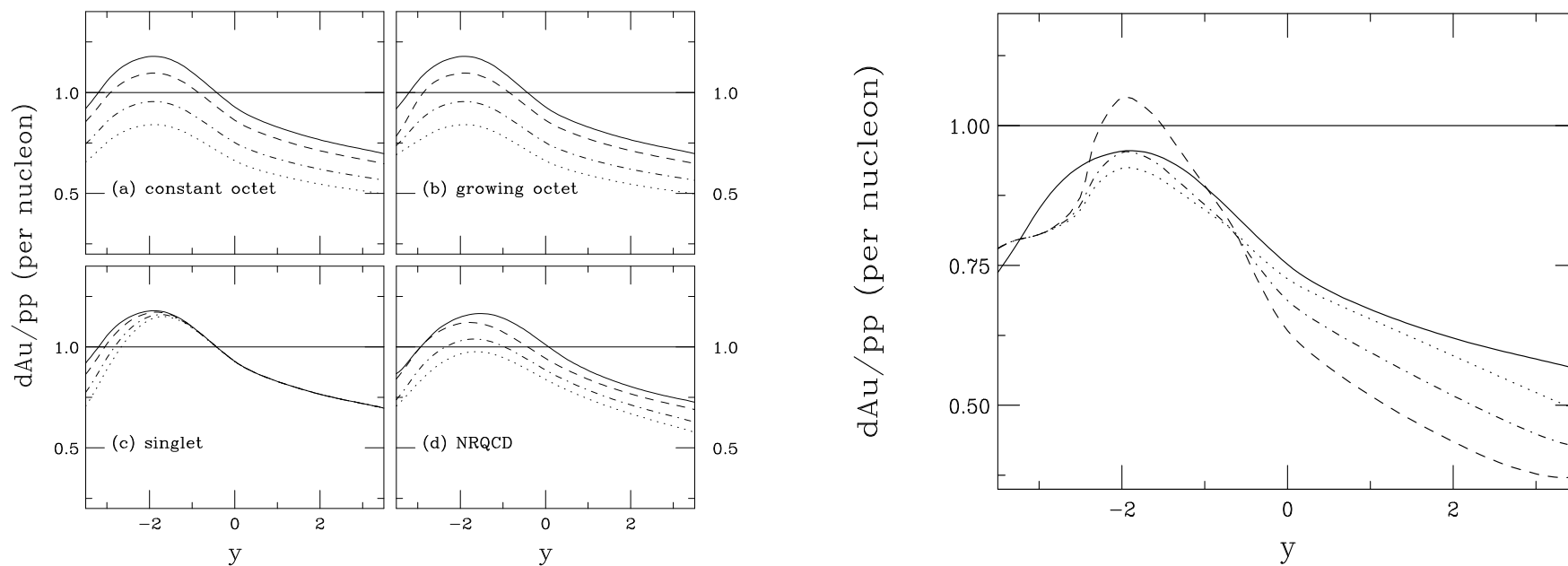


Figure 35: Left-hand side: The J/ψ $d\text{Au}/pp$ ratio at 200 GeV with the EKS98 shadowing parameterization as a function of rapidity for our absorption models: (a) constant octet, (b) growing octet, (c) singlet and (d) a combination of octet and singlet. In (a)-(c), the curves are no absorption (solid), $\sigma_{\text{abs}} = 1$ (dashed), 3 (dot-dashed) and 5 mb (dotted). In (d), the results are no absorption (solid), 1 mb octet/1 mb singlet (dashed), 3 mb octet/3 mb singlet (dot-dashed), and 5 mb octet/3 mb singlet (dotted). Right-hand side: Comparison of the results for a 3 mb growing octet absorption cross section with the EKS98 (solid), FGS0 (dashed), FGS1 (dot-dashed) and FGS2 (dotted) shadowing parameterizations.

Inhomogeneous Shadowing and Absorption

PHENIX results presented as a function of N_{coll} , the convolution of the nuclear profile functions multiplied by the inelastic NN cross section, 42 mb at RHIC

$$N_{\text{coll}}(b) = \sigma_{NN}^{\text{in}} \int d^2s T_A(s) T_B(|\vec{b} - \vec{s}|)$$

Results with EKS98 compared at $y = -2$ (antishadowing), 0 (transition region) 2 (shadowing)

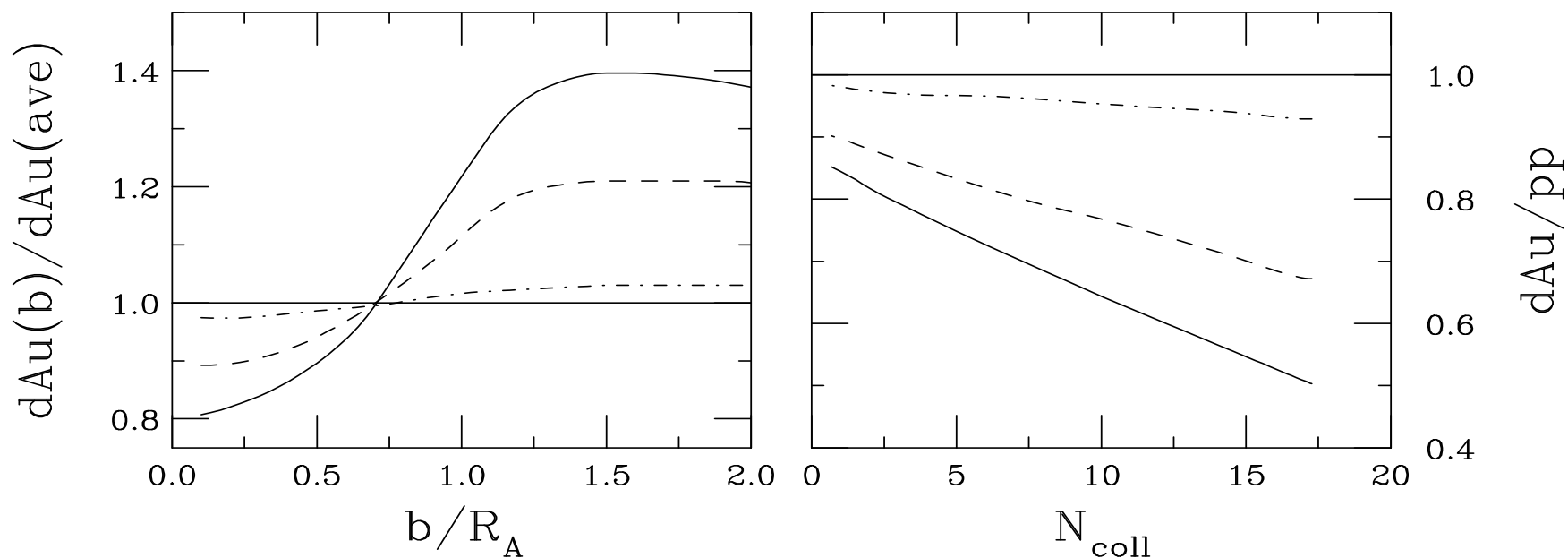


Figure 36: Left-hand side: The J/ψ ratio $(dAu(b)/pp)/(dAu(\text{ave})/pp)$ as a function of b/R_A . Right-hand side: The ratio dAu/pp as a function of N_{coll} . Results are shown for $y = -2$ (dot-dashed), $y = 0$ (dashed) and $y = 2$ (solid) at 200 GeV for a growing octet with $\sigma_{\text{abs}} = 3$ mb and the EKS98 parameterization.

Comparison of N_{coll} Dependence

Path length parameterization, $S_{P,\rho}$, with EKS98 and FGSo gives linear N_{coll} dependence due to long tails of density distributions

FGSh and FGSI forced to $S = 1$ at $b = 10$ fm so that as $N_{\text{coll}} \rightarrow 1$, shadowing disappears and only residual absorption remains

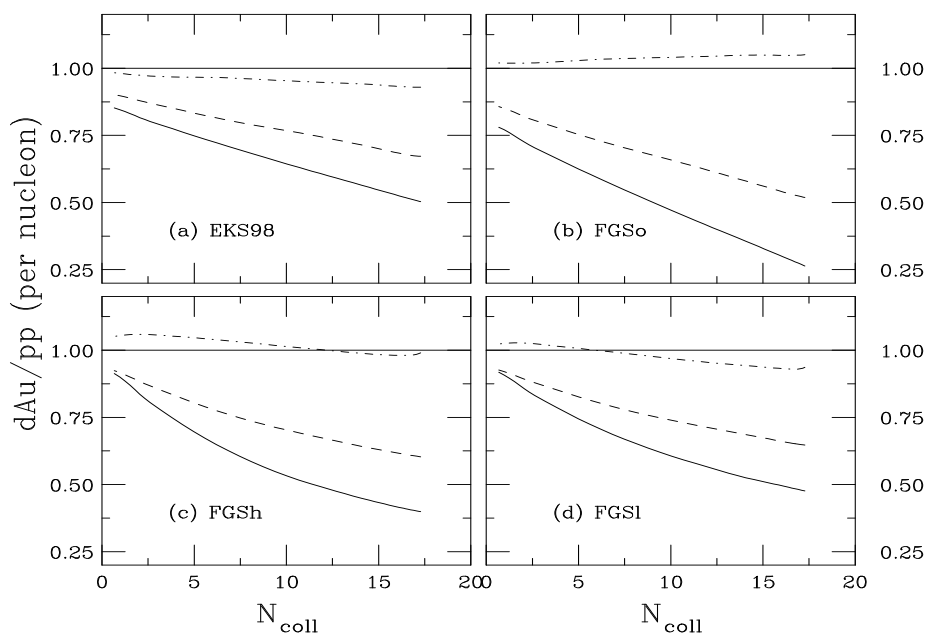


Figure 37: The ratio dAu/pp as a function of N_{coll} for the EKS98 (a), FGSo (b), FGSh (c) and FGSI (d) shadowing parameterizations. The calculations with EKS98 and FGSo use the inhomogeneous path length parameterization while that obtained by FGS is used with FGSh and FGSI. Results are given for $y = -2$ (dot-dashed), $y = 0$ (dashed) and $y = 2$ (solid) at 200 GeV for a growing octet with $\sigma_{\text{abs}} = 3$ mb.

Summary

- Theoretical uncertainty bands for charm must be constructed carefully due to low x and low μ behavior of parton densities
- This influences how well we can extrapolate to higher energies
- More modern fragmentation functions for D and B mesons indicate that the meson distribution is more similar to the quark distribution to higher p_T than previously assumed from older e^+e^- fits
- Contributions of D and B decays to leptons difficult to disentangle and would require precision measurements of their decays to hadrons to better distinguish
- More and better understood data will help complete this picture – perhaps easier to obtain with better triggers, efficiencies, and higher luminosities